

Thesis

BELFKIR Mohamed

December 2020

Contents

1	Introduction	6
2	Theoretical Framework	7
2.1	Introduction	7
2.2	Standard Model (SM) of particle physics	8
2.2.1	Elementary Particles	8
2.2.2	Elementary Interactions	9
2.3	Electroweak Symmetry Breaking (EWSB)	12
2.4	Higgs Boson Discovery	13
2.4.1	p-p collisions	14
2.4.2	Higgs boson production	15
2.4.3	Higgs boson decay channels	18
2.4.4	Higgs measurements	19
2.5	Double Higgs boson	22
2.5.1	Di-Higgs production and decays	22
2.5.2	Di-Higgs as a probe of BSM physics	25
2.5.3	Current Measurements	27
2.6	Effective Field Theory (EFT)	28
2.7	Conclusion	29
3	The Large Hadron Collider and the ATLAS detector	30
3.1	The Large Hadron Collider	30
3.1.1	Acceleration chain	31
3.1.2	Luminosity	32
3.1.3	Pile-up	32
3.2	ATLAS A Toroidal LHC ApparatuS detector	34
3.2.1	Coordinated system	34
3.2.2	The Inner Tracker	35
3.2.3	Calorimeter system	39
3.2.4	Muon Spectrometer	43
3.2.5	Trigger	44
3.3	Physics objects reconstruction	45
4	Photons in ATLAS	46
4.1	Photons Reconstruction	46
4.2	Photons Isolation	46
4.3	Photons Identification	46

4.4	Shower shape mis-modelling	46
4.5	Convolutional Neural Network for Photon Identification	46
4.6	Conclusion	47
5	Other Objects in ATLAS	48
6	Experimental Setup for Self-coupling measurement	49
7	Conclusion	50
8	Appendix 1	51

List of Figures

2.1	Shape of the Higgs potential for $\mu^2 < 0$ this potential has an infinite amount of minima. [5]	12
2.2	The χ^2 function for the SM as a function of the Higgs mass, LEP and Tevatron exclusions limits are shown.	14
2.3	The CT14 PDFs at $Q=2$ GeV (left) and $Q = 100$ GeV (right) for different partons. These PDFs are computed at next-to-next-to-leading order.	15
2.4	Feynman diagrams for the main production modes of Higgs boson.	15
2.5	Cross sections for different Higgs boson production modes at a proton-proton collider with a centre-of-mass energy of 6-15 TeV (a). A Higgs mass of 125 GeV is assumed in this plot. Additionally, cross sections as a function of Higgs mass are shown (b) [12].	17
2.6	Higgs boson total decay width as a function of Higgs mass [13].	18
2.7	Higgs boson branching ratio of the possible Higgs decay channels as a function of the Higgs mass [14]	18
2.8	Feynman diagrams of the $H \rightarrow \gamma\gamma$ decay. Other particles can also propagate in the loop.	19
2.9	Weighted distributions of the invariant mass of di-photon [16].	20
2.10	The observed local p-value as a function of m_H (solid line) and the expectation with its $\pm 1\sigma$ band assuming the presence of a Standard Model Higgs boson at that mass (dashed line) from the combination of the ZZ^* , $\gamma\gamma$ and WW^* channels by the ATLAS experiment. The horizontal dashed lines indicate the p-values corresponding to significances of 1 to 6σ [16].	20
2.11	The inclusive diphoton invariant mass distribution [19].	21
2.12	Cross sections times branching fraction for $ggF + b\bar{b}H$, VBF , VH and $t\bar{t}H + tH$ production, normalized to their SM predictions [19].	21
2.13	The particle content of the Standard Model (SM).	22
2.14	Leading Order (LO) Feynman diagrams contributing to ggF Higgs boson pair production through a top-quark loop (box) and through the triple self-coupling of the Higgs boson (triangle).	23
2.15	Total cross sections at the NLO for HH production as a function of centre-of-mass energy. Assuming κ_λ and κ_t equals to their SM values.	23
2.16	HH production modes, in decreasing order of cross section. λ refers to Higgs tri-linear coupling: (a) ggF mode, (b) VBF mode, (c) Vector boson association (VH) and (d) top associated production.	24
2.17	Di-Higgs system decay branching ratios assuming SM Higgs bosons with $m_H = 125.09$ GeV.	25
2.18	Illustration of both box and triangle diagrams contribution to di-Higgs invariant mass spectrum.	26
2.19	Higgs pair invariant-mass distribution in ggF for various values of κ_λ assuming $\kappa_t = 1$	27

2.20 Total LO and NLO cross sections for HH production at the LHC with $\sqrt{s} = 14$ TeV, as a function of the self-interaction coupling κ_λ	27
2.21 The expected and observed 95% CL limits on the non-resonant production cross section $\sigma_{gg \rightarrow HH}$ as a function of κ_λ . The red line indicates the predicted HH cross section if κ_λ is varied but all other couplings remain at their SM values. The red band indicates the theoretical uncertainty of this prediction.	28
3.1 Overview of the CERN accelerator complex, including the LHC and its pre-accelerators [27]. The four main LHC experiments are depicted, too	31
3.2 Luminosity delivered by the LHC during the Run 2 data taking. ATLAS recorded this data with an efficiency above 90%.	33
3.3 Mean number of interaction per bunch crossing in pp collisions recorded by the ATLAS detector during Run 2 at 13 TeV [28].	33
3.4 Sketch of the ATLAS detector with its different sub-detectors.	34
3.5 Coordinate system used by the ATLAS and CMS experiments at the LHC.	35
3.6 Layout of the Inner Detector (ID), including the new Insertable B-Layer (IBL) [32].	36
3.7 (a) Transverse view of 3 of the Insertable-B-Layer (IBL) staves, located directly on the beam pipe. (b) The layout of one of the 14 IBL staves [32].	37
3.8 Unfolded longitudinal impact parameter resolution measured from data in 2015, $\sqrt{s} = 13$ TeV, with the Inner Detector including the IBL, as a function of η for values of $0.4 \leq p_T \leq 0.5$ GeV compared to that measured from data in 2012, $\sqrt{s} = 8$ TeV [34].	37
3.9 The average efficiency to reconstruct primary tracks with a production vertex before the first layer in jets as a function of jet p_T . The same sample generation, with limited statistics, is used for both reconstruction algorithms resulting in correlated features [36].	38
3.10 Rejection factor against light jets as a function of b -jet efficiency for the combined IP3D+SV1 tagger. Compared are the results with and without IBL.	38
3.11 The Perigee representation of the track [39].	40
3.12 ATLAS Calorimeter system.	40
3.13 Accordion shape of the EM calorimeter.	41
3.14 Side view of one quadrant (<i>right</i>) and transverse view (<i>left</i>) of the muon spectrometer.	43
3.15 Transverse cross section of the MDT tube.	44

List of Tables

2.1	Generations of quarks and leptons with their masses and electrical charges	9
2.2	The 95% CL observed and expected limits on the Higgs boson pair cross-section in pb and as a multiple of the SM production cross-section. The $\pm 1\sigma$ band around each 95% CL limit is also indicated.	28
3.1	Granularity of the EM calorimeter ($\Delta\eta \times \Delta\phi$) [40].	42

Introduction

Theoretical Framework

This chapter should contains all theory needed for SM:

- Describe the elementary particles
- Describe the fundamental interactions and their related fields
- Describe the EWSB and Higgs physics introduction
- Brief introduction to p-p collision and higgs production at LHC
- Discovery of Higgs boson at CERN 2012
- Higgs self coupling anomaly
- Describe Di-Higgs production as a direct process to measure higgs self coupling and probe of BSM effects
- Early Run 2 results and limits on κ_λ
- Introduction to EFT as an alternative interpretation of Full Run 2 results to probe physics at large scale

2.1 Introduction

This section should include a brief history of particle physics and the SM.

How the world around us made? How does it work? These are questions asked a long-ago to understand the Universe. The first efforts to elucidate those questions referred to ancient Greek philosophers. Greeks gave much to the physics by developing the fundamental basis of modern principles as the conservation of matter, atomic theory. Democritus's model introduced Atom as small indivisible building blocks (particles) that matter consists off. At that time, atoms allowed to describe a variety of phenomena. Rutherford came in 1909 with his experience saying that atoms consist of mostly space with Electrons surrounding a dense central nucleus made up of Protons and Neutrons. At that time, Newtonian laws of motion and atoms provided a solid framework. A continuing collaboration between theorists and experimentalists brought us to a simple theory upon which all modern physic the Standard Model (SM). Currently, SM is the most accurate model describing the universe composition. In the SM, there are two types of elementary particles: fundamental constituents of matter called "Fermions", and the quanta of fields called "Bosons" exchanged between when an interaction occurs between fermions. The SM has been successfully, so far, at predicting the results from the measurements performed in the past 50 years. The following sections provide more details about the Standard Model and its particles.

2.2 Standard Model (SM) of particle physics

One of the physicist goal is to describe all natural phenomena with a minimal set of fundamental laws and theories which, at least in principle, can quantitatively explain and predict experimental results. At the microscopic scale, all matter behaviour and phenomenology, including molecular, atomic, nuclear, and subnuclear physics, can be explained under three fundamental interactions: electromagnetic, weak and strong forces. At the macroscopic scale, the fourth force, the gravitational interaction, has an essential role, while it is negligible at the microscopic scale. All the three interactions are described within a local relativistic Quantum Field Theory (QFT) based on the principal gauge invariance of $SU(3)\times SU(2)\times U(1)$. This is called "The Standard Model". Within the SM matter consists of fermions and interactions are mediated by bosons.

2.2.1 Elementary Particles

This should include a description of elementary particles, Fermions and Bosons and their properties (mass, spin, charge, quantum number)

In the SM, particles are classified as either fermions or bosons depending on what statistics they obey. Fermions obey Fermi-Dirac statistics and respect the Pauli exclusion principle, i.e. two fermions in the same quantum state can not exist in the same place and time. Such particles have an intrinsic angular momentum, called spin J equal to half-integer. Bosons obey Bose-Einstein statistics, due to spin-statistics theorem, corresponding to integer spin value. Through an interaction, a boson emitted by a matter particle and then absorbed by another particle. Fermions are divided into two categories: Leptons and Quarks.

Leptons

Leptons (comes from the Greek word meaning "light") are grouped into three families or generations formed by three charged leptons: electron e , muons μ and tau τ with electric charge $-e$, where e is equal to the elementary electric charge of $\sim 1.6 \cdot 10^{-19} C$ [1], and their neutral complemented partners neutrinos : ν_e , ν_μ and ν_τ . Only electron and neutrinos are stable. A quantum number called Leptonic number (L) is associated with each lepton. Electron, muon and tau have identical properties (a charge, spin) however tau is 3477 times heavier than an electron while the muon is only 17 times the mass of an electron. The rest mass of an electron is $9.10938356 \cdot 10^{-31} Kg$. From 20 May 2019 kilogram not anymore part of the International System of Units for that masses will be expressed by the unit of energy (E) the electron-volt (eV) in this thesis. Mass is related to eV by the equation $E = mc^2$, c being the velocity of light in vacuum. In particle and high energy physics, c is fixed to one. Electron mass is $511 keV$.

Quarks

Quarks are electrically charged particles, with charge of $+\frac{2}{3}e$ for so-called up-type quarks and $-\frac{1}{3}e$ for the down-type quarks. There are six known quark flavours, similarly to leptons, quarks are paired into three generations. The first generation consists of up (u) and down (d) quarks, the second has the charm (c) and strange (s) quarks, and top (t) and bottom (b) quarks for the third generation. Quarks can not exist in a free state due to the QCD color confinement. Table 2.1 shows a summary of leptons and quarks.

For both quarks and leptons each of the higher generations has particles with higher mass and tends to

decay to the lower one, explains why the ordinary matter made off the first-generation particles. Each fermion has it associated to a corresponding anti-particle.

	1st Generation	2nd Generation	3rd Generation
Quarks	u 2.16 MeV $+\frac{2}{3}$	c 1.27 GeV $+\frac{2}{3}$	t 172.4 GeV $+\frac{2}{3}$
	d 4.67 MeV $-\frac{1}{3}$	s 93 MeV $-\frac{1}{3}$	b 4.18 GeV $-\frac{1}{3}$
Leptons	e 0.511 MeV -1	μ 105.7 MeV -1	τ 1.8 GeV -1
	ν_e 0 0	ν_μ 0 0	ν_τ 0 0

Table 2.1: Generations of quarks and leptons with their masses and electrical charges

Standard Model of elementary particles assumes neutrinos to be mass-less particles, while some experiments demonstrate that neutrinos have a non-negligible mass $\sim eV$, which makes it an incomplete theory.

Bosons

As mentioned before, bosons are particles of integer angular momentum and obey to the Bose-Einstein statistics. They are the carriers of the gauge interactions between fermions. Photon (γ) is a boson known as a quantum of the electromagnetic field including electromagnetic radiation such as light. Photons are neutral and mass-less particles. W^\pm, Z^0 are bosonic particles wish carriers the weak interaction. Z^0 boson is neutral while W^\pm charged with a charge of $\pm e$. Contrary to photons, Weak bosons are massive. W^\pm and Z^0 masses are predicted to be so large that it took many years to build powerful accelerators to produce them. W^\pm and Z^0 bosons have been directly discovered at CERN in 1983 by the UA1 and UA2 collaborations [2, 3] and predicted at the end of 1972 by the charged (CC) and neutral currents (CN) of the weak interaction, and their masses were found to be about 80 GeV and 91 GeV respectively. Gluons are the neutral quantum of the strong force known as the "glue" that links quarks to form hadrons. The mass of the gluons is known to be strictly zero. There are eight gluons.

2.2.2 Elementary Interactions

This should include a description of the 4 interaction and their properties.

The associated group for each of the SM interactions (U(1) SU(2) SU(3)) and the its Lagrangian.

How SM combines the 3 groups in one fundamental theory which describe particle physics.

Brief summary of boson vs interactions

At the microscopic level, there are three fundamental forces: electromagnetic, weak and strong. The interactions relate to matter (fermions) by the transmission of a boson. The SM content and interactions can be expressed more formally through the concepts of symmetries and gauge invariance. Each interaction is described through a gauge group. The generators of the group correspond to the gauge bosons

that are mediators of the fundamental force and responsible for the interactions. The electromagnetic interaction mediated by photons, the weak force used W^\pm and Z^0 as mediators, while the Gluons are mediators for the strong interaction.

Electromagnetic interaction

Electromagnetic interaction describes the dynamics of electrically charged fermions. It is described by the Quantum Electrodynamics (QED). Each quantum field theory is represented by a Lagrangian density. The QED Lagrangian representing the behaviour of a freely propagating fermion field $\psi(x, t)$ can be written as :

$$\mathcal{L} = \bar{\psi} i\gamma^\mu \partial_\mu \psi - m\psi\bar{\psi}, \quad (2.1)$$

where m is the mass of the particle. The Einstein convention is used here, with the indices $\mu = 0, 1, 2, 3$ representing the space-time components x and t .

To be a valid gauge theory the QED lagrangian should be invariant under a $U(1)$ (electromagnetic force group) local gauge transformation of the field : $\psi \rightarrow e^{i\alpha(x)}\psi$. This condition leads to additional terms to be added to the lagrangian and new gauge field A_μ that represents the photon:

$$\mathcal{L}_{QED} = \bar{\psi} i\gamma^\mu \partial_\mu \psi - m\psi\bar{\psi} + q\psi\gamma^\mu\psi A_\mu - \frac{1}{4}F^{\mu\nu}F_{\mu\nu}, \quad (2.2)$$

where $F^{\mu\nu} = -F^{\nu\mu} = \partial^\nu A^\mu - \partial^\mu A^\nu$ is the field-strength tensor for the electromagnetic force describes the kinetic propagation of the field. Note that $U(1)$ is an Abelian group which means that photons can not self-interact and the EM tensor does not have the photon self-interaction term included. The term $q\psi\gamma^\mu\psi A_\mu$ reflects the interaction between a fermion and the electromagnetic force (photon) with strength q ($q=-e$) the electromagnetic interaction charge (electric charge). The mass term of the photon is not added to the lagrangian since it spoils the gauge invariance. This is in agreement with the observation that the photon is mass-less. $U(1)$ has one generator which corresponds to the photon mediator.

Electro-Weak interaction

Electroweak interaction consists of an unification of the electromagnetic and weak interactions. It is described by the combined gauge symmetry $SU(2)_T \times U(1)_Y$, where the $U(1)_Y$ symmetry mimics that of QED with the weak hypercharge Y . The $SU(2)$ represents the weak interaction with its generator vector T called weak isospin. The Lagrangian of the theory can be written as :

$$\mathcal{L}_{EW} = \bar{\psi} i\gamma^\mu \partial_\mu \psi - eY\bar{\psi}\gamma^\mu B_\mu \psi - g_W\bar{\psi}\gamma^\mu \mathbf{T} \cdot \mathbf{W}_\mu \psi - \frac{1}{4}F^{\mu\nu}F_{\mu\nu} - \frac{1}{4}W^{i\mu\nu}W_{\mu\nu}^i, \quad (2.3)$$

where g_W is the weak coupling to the fermionic fields. The first two terms are similar to \mathcal{L}_{QED} . However, the term representing the coupling of fermions to photons is replaced by more general terms: the W_μ field and the hyper-photon B_μ field. The two charged vector bosons W^\pm appear as linear combinations of the W_μ field components, $W_\mu^\pm = \frac{1}{\sqrt{2}}(W_\mu^1 \mp W_\mu^2)$. The photon is now created through the mixing of the W_μ and B_μ fields, as :

$$A_\mu = B_\mu \cos\theta_W + W_\mu^3 \sin\theta_W, \quad (2.4)$$

where θ_W is the weak mixing angle, and the Z_μ field, corresponding to the Z boson, is generated similarly as :

$$Z_\mu = -B_\mu \sin\theta_W + W_\mu^3 \cos\theta_W. \quad (2.5)$$

The field strength tensor for the weak gauge fields W^i is defined as:

$$W_{\mu\nu}^i = \partial_\mu W_\nu^i - \partial_\nu W_\mu^i - g_W \epsilon_{ijk} W_\mu^j W_\nu^k, \quad (2.6)$$

The non-Abelian nature of $SU(2)$ generates the third term in Eq.(2.6), which gives rise to the weak boson self-interactions.

The electric charge q is related to Y and T by through the Gell-Mann-Nishijima relation:

$$q = T_3 + \frac{Y}{2}, \quad (2.7)$$

where T_3 is the third component of the isospin T . Fermions are decomposed into left-handed and right-handed chirality types. The chirality is defined for mass-less particles as the same as helicity and refers to the relation between the spin and momentum direction. While for massive particles chirality is trickier to define. Note that the electroweak force interacts only with left-handed particles because interaction with right-handed particles would violate the parity. The chirality separates between left-handed doublets, and the right-handed singlets:

$$(\nu_i \ i)_L^T, \ i_R \text{ with } i = e, \mu \text{ or } \tau, \quad (2.8)$$

and,

$$(u \ d)_L^T, \ (c \ s)_L^T, \ (t \ b)_L^T, \ u_R, \ d_R \dots . \quad (2.9)$$

Strong interaction

Additionally to QED, the strong interaction is described by Quantum Chromo-Dynamics (QCD), which is a local gauge symmetry under $SU(3)_C$. $SU(3)$ has eight generators corresponding to the eight gluons mediators of the strong force. The expression for the locally gauge invariant Lagrangian of the QCD, which describes interactions of quarks of mass m and quark-field spinors ψ via a mass-less gluons is:

$$\mathcal{L}_{QCD} = \sum_{flavours} \bar{\psi}_a (i\gamma^\mu \partial_\mu \delta_{ab} - g_s \gamma^\mu t_{ab}^C G_\mu^C - m \delta_{ab}) \psi_b - \frac{1}{4} F_{\alpha\beta}^A F^{A\alpha\beta}, \quad (2.10)$$

where $a = 1, 2, 3$ is the color index. The G_μ^C are the gluon fields with $C = 1, 2, \dots, 8$ that transform under the adjoint representation of the $SU(3)$ group. The t_{ab}^C are the generators of the $SU(3)$ group, the quantity g_s corresponds to strong coupling constant that determines the strength of interactions between coloured particles (quarks and gluons). The strong field tensor is defined as :

$$F_{\alpha\beta}^A = \partial_\mu G_\nu^A - \partial_\nu G_\mu^A - g_s f^{ABC} G_\mu^B G_\nu^C, \quad (2.11)$$

where f^{ABC} are the structure constants of the $SU(3)$ group. In contrast to QED, the field tensor of the QCD includes the gluon triplet and quartic self-interactions. Only particles carrying colour charge (i.e. quarks) couple to these gluons. Colour charge is conserved in each interaction. Since the $SU(3)$ group is non-Abelian, the gluons themselves must also carry (anti-)colour charge and thus interact with each other.

Finally, the Standard Model Lagrangian density could be summarized as :

$$\mathcal{L}_{SM} \sim \mathcal{L}_{EW} + \mathcal{L}_{QCD}. \quad (2.12)$$

Note that, in the \mathcal{L}_{EW} no mass term is introduced for the two newly appearing bosons, while experimental observations were indicates large masses. Additionally, the fermion mass term that appeared in \mathcal{L}_{QED} is now absent in \mathcal{L}_{EW} , requiring the introduction of an additional mechanism to explain the origin of their mass. This is handled through the process of Electroweak Symmetry Breaking (EWSB), and the introduction of the Higgs mechanism to generate mass.

2.3 Electroweak Symmetry Breaking (EWSB)

This section will ask the question mass of particles and introduce the EWSB to answer.

Introduce the Higgs boson and its properties.

The gauge bosons mass terms cannot be simply introduced as it would break gauge invariance. Brout-Englert-Higgs (BEH) mechanism introduces a spontaneous symmetry breaking ad-hoc in the SM to preserve the local gauge invariance [4]. In the minimal model of EWSB, mass of particle can be generated by introducing the Higgs field represented by a weak iso-spin doublet of one charged and one neutral complex scalar ($J=0$) field complex scalar :

$$\phi(x) = \frac{1}{\sqrt{2}} \begin{pmatrix} \phi_+ \\ \phi_0 \end{pmatrix}. \quad (2.13)$$

Higgs lagrangian is added to the SM lagrangian as :

$$\mathcal{L}_{\text{Higgs}} = (D^\mu \phi)^\dagger (D_\mu \phi) - V(\phi), \quad (2.14)$$

where D^μ is the covariant derivative $D^\mu = (\partial_\mu + igT^i W_\mu^i + i\frac{1}{2}g'B_\mu)$. The kinetic and the interaction of the Higgs field with weak gauge bosons is described by the term $D^\mu \phi$. $V(\phi)$ is the Higgs potential:

$$V(\phi) = \mu^2 \phi^+ \phi + \lambda (\phi^+ \phi)^2, \quad (2.15)$$

the first term can be associated to the mass of the field and the second represents the quadratic self-interaction of the scalar field. The parameter λ has to be positive to obtain a potential with finite minima, while μ can be chosen freely. For $\mu^2 > 0$, the potential has a single ground state at zero with all fields being zero ($\phi_0 = 0$). Hence the vacuum expectation value of the Higgs field would be zero and the symmetry is preserved. However, for $\mu^2 < 0$ the potential has an infinite set of minima v given by :

$$\phi_0 = \langle \phi^+ \phi \rangle = \frac{v^2}{2} = -\frac{\mu^2}{2\lambda}, \quad (2.16)$$

$v \neq 0$ being the vacuum expectation value (vev) which is illustrated in Figure 2.1.

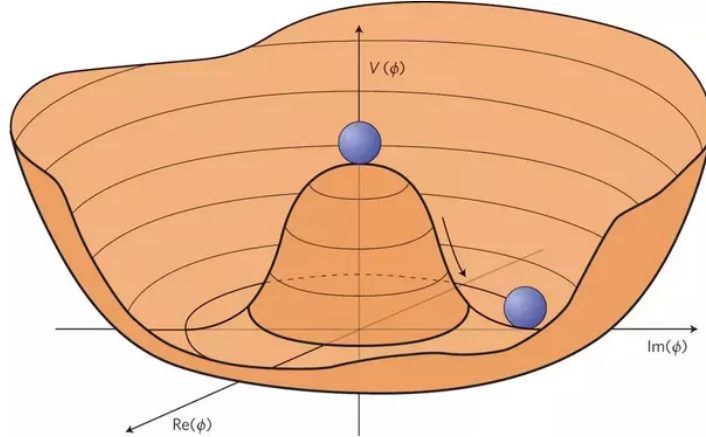


Figure 2.1: Shape of the Higgs potential for $\mu^2 < 0$ this potential has an infinite amount of minima. [5]

The choice of the physical vacuum state spontaneously breaks the Lagrangian symmetry. An expansion of ϕ_0 around its vacuum state v introduces a massive scalar and three mass-less Gladstone bosons.

However, the Goldstone bosons appear to be not physical and can be eliminated using the gauge Unitary, enforcing the Higgs doublet to be real:

$$\phi(x) = \frac{1}{\sqrt{2}} \begin{pmatrix} 0 \\ v + h(x) \end{pmatrix}, \quad (2.17)$$

where $h(x)$ is physical field linked to the Higgs boson. The form of Higgs potential becomes:

$$V(\phi) = -\frac{1}{2}m_H^2 h^2(x) + \lambda_{HHH} h^3(x) + \lambda_{HHHH} h^4(x), \quad (2.18)$$

where $m_H^2 = 2\lambda^2 = 2\lambda v^2$ is the square of Higgs mass, λ_{HHH} is the coupling in a vertex with tree Higgs and λ_{HHHH} for the case of four Higgs. Accordingly, the terms giving the mass to the gauge bosons can be identified:

$$m_W = \frac{1}{2}gv \quad (2.19)$$

$$m_A = 0 \quad (2.20)$$

$$m_Z = \frac{m_W}{\cos \theta_W}. \quad (2.21)$$

The Higgs mechanism associates the degrees of freedom of hypothetical scalar (Goldstone) bosons with the longitudinal components of gauge bosons and consequently become massive. The coupling of the Higgs boson to the gauge bosons appears to be proportional to the gauge boson masses. The mass of the fermions not explained in the same way as the fermions acquire masses through the corresponding Yukawa couplings. Weak bosons masses are predicted in the SM, while Higgs boson mass is unknown and could have any value. Higgs mass needs to be measured, and the Higgs boson discovery is necessary to confirm the EWSB [6].

2.4 Higgs Boson Discovery

This should contains the story of Higgs boson discovery by ATLAS and CMS in 2012.

The Large Electron Positron (LEP) collider approved by the CERN Council in 1981 and commissioned eight years later, provides a detailed study of the electroweak interaction for 11 years of research. Results from LEP are used to perform stringent tests of the SM by comparing the precise results with theory predictions. LEP allows us to measure the masses of heavy fundamental particles, such as the top quark and the W boson, which are then compared to the predictions. This checks the correctness of the SM predictions. Constraining the Higgs mass is a particular interest, because this fundamental ingredient of SM has not been observed and needed to complete the SM picture. At the beginning of the LEP program no solid limit existed on the mass of the Higgs boson. The searches for the SM Higgs boson carried out by the four LEP experiments extended the sensitive range well beyond that anticipated at the beginning of the LEP program. Similarly, the Tevatron experiments CDF and D0 have excluded a range of mass $162 < m_H < 166$. Figure 2.2 shows the LEP and Tevatron exclusion limits [7, 8, 9]. A combined fit to all the data shown in 2.2 yields to the best estimated Higgs mass at that time of $m_H = 116.4^{+15.6}_{-1.3}$ GeV. This is due to the higher energy achieved and to more sophisticated detectors and analysis techniques. However, circular accelerators with electrons is limited by synchrotron radiation due to the small electron mass. Since muon acceleration is not possible at the current stage due to the short life time of muons, proton collisions represent a good way to achieve high-energy collisions needed for Higgs discovery. LEP was closed down on 2 November 2000 to make way for the construction of the

Large Hadron Collider (LHC) in the same tunnel. LHC provides a nominal proton-proton collisions at a centre-of-mass energy of $\sqrt{(s)}$ up to 14, while at the beginning of LHC the energy was 7-8 TeV and during last 4 years the maximal achieved energy is 13 TeV. LHC is detailed in a dedicated Chapter 3.

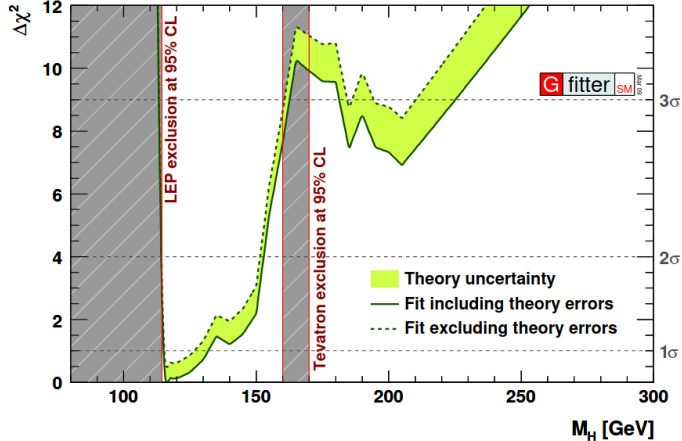


Figure 2.2: The χ^2 function for the SM as a function of the Higgs mass, LEP and Tevatron exclusions limits are shown.

2.4.1 p-p collisions

The protons protons collision and the Higgs boson cross section at 8 TeV and 13 TeV.

Protons are fermions known to be made up of two up and one down quarks (uud) called valence quarks. They interact between each other through the strong force via gluon exchange. Due to nature of QCD (non-abelian) gluons can fluctuate into quark anti-quark pairs forming the so-called sea quarks. Effectively, a proton is therefore a bound state of quarks and gluons called partons each carries a fraction x of the total proton momentum. At LHC process are produced by colliding mainly protons beams, similarly Higgs boson processes are in p-p collision.

$$p_1 + p_2 \rightarrow h. \quad (2.22)$$

The probability for a process to occur is expressed in terms of its cross section, and the dynamics of its products is determined by the dynamics of partons involved in the collision. The hard scattering cross section for such process is given by :

$$d\sigma^{p_1 p_2 \rightarrow h} = \int_0^1 dx_1 \int_0^1 dx_2 \sum_{a,b} f_{a/p_1}(x_1, \mu_F^2) f_{b/p_2}(x_2, \mu_F^2) d\hat{\sigma}^{ab \rightarrow h}(x_1, x_2, \mu_F^2), \quad (2.23)$$

where a, b are the partons involved in the process and $f_{n/p_i}(x_i)$ is the parton distribution function (PDF), which is the probability to find a parton of type n inside proton p_i with a longitudinal momentum fraction x_i at energy scale Q . $\sigma^{ab \rightarrow h}$ is the parton cross section of the process.

In general, the x dependence at a given Q^2 cannot be calculated analytically but rather are extracted from global fits to data from many experiments. There are different PDF sets which use different fitting methods and experimental data [10]. Figure 2.3 shows two examples of CT14 PDFs at given Q^2 computed using use of data from LHC experiments, and the new DØ charged lepton rapidity asymmetry data [11].

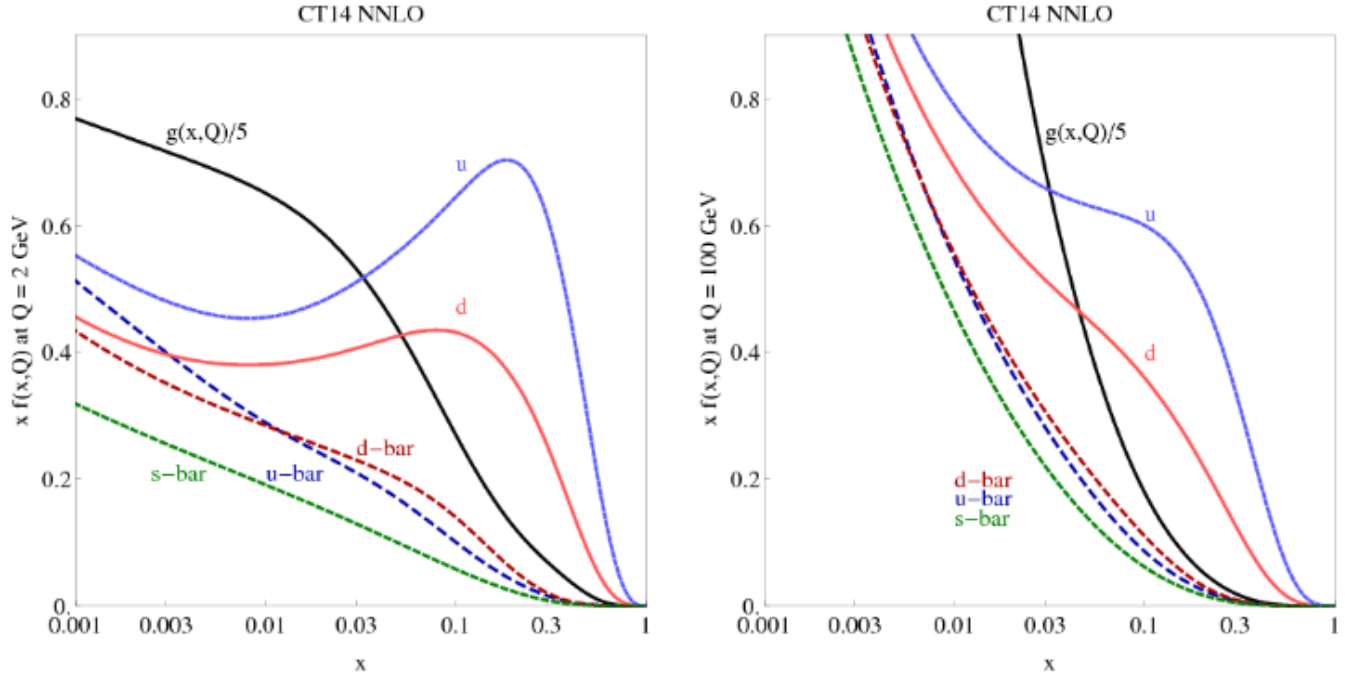


Figure 2.3: The CT14 PDFs at $Q=2$ GeV (left) and $Q=100$ GeV (right) for different partons. These PDFs are computed at next-to-next-to-leading order.

The production of the Higgs boson at the LHC occurs in different modes. Their cross sections depend on the coupling of the Higgs boson to specific particles, but also essentially on the PDFs described above.

2.4.2 Higgs boson production

Higgs boson production modes ggF VBF VH and qqH.

The main process contributing to the Higgs boson production at LHC are represented by their leading Feynman diagrams in Figure 2.4. The most important Higgs production mode occurs via fusion of gluons (ggF).

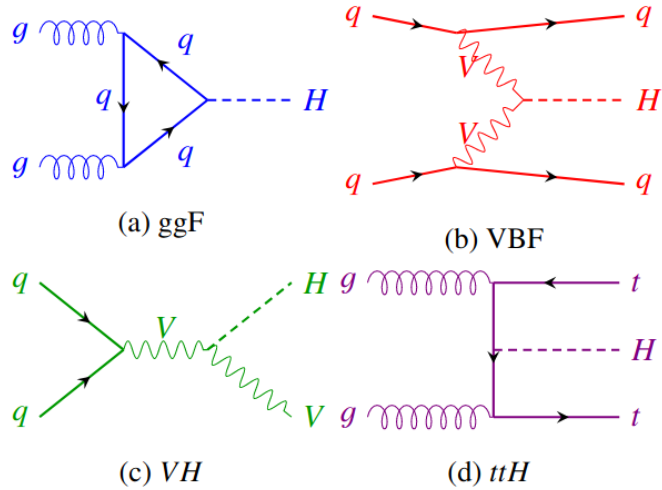


Figure 2.4: Feynman diagrams for the main production modes of Higgs boson.

In order of decreasing cross section, the Higgs boson production modes are:

- gluons-gluons fusion (ggF) : the main Higgs boson production at LHC over the whole mass spectrum. The process involves the fusion of two incoming gluons that give rise to the Higgs boson through a heavy quark loop, whose main contribution comes from the top quark, as shown in Figure 2.4 (a).
- Vector Boson Fusion (VBF) : each of the two interacting quarks emit a W or Z boson which, in turn, interact to produce the Higgs boson, as shown in figure 2.4 (b). Quarks deriving from the incoming partons after the emission of vector bosons proceed in the forward direction and represent the peculiar signature of this production mode, two high energy forward jets separated by a large pseudo-rapidity gap, a $\Delta\eta$ region with reduced particle density. This process has a cross section which is one order of magnitude lower than ggF for a large range of Higgs boson mass (m_H) values and it becomes comparable to ggF only for masses of the order of 1 TeV as shown in Figure 2.5 (b).
- Vector boson associated production (VH) : also known as Higgs strahlung, this process is characterized by the emission of a Higgs boson from a W^\pm or Z boson produced by two incoming quarks, as shown in figure 2.4 (c). The VH cross section is several orders of magnitude lower than the ggF and VBF cross sections for m_H larger than about 300 GeV, while the VH and VBF cross sections are comparable around $m_H = 125$ GeV as shown Figure 2.5 (b).
- Top quark associated production ($t\bar{t}H$) : a pair of top quarks, originated from the splitting of two incoming gluons, interacts to give rise to a Higgs boson, as shown in figure 2.4 (d). the production in association with a pair of top quarks allows a direct measurement of the Higgs boson coupling to the top quark. Another production mechanism analogous to the $t\bar{t}H$ process and with a similar cross section is the b-quark associated production.

The SM Higgs boson production cross section for the various production modes depends on the Higgs boson mass and on the center-of-mass energy, as shown in Figure 2.5.

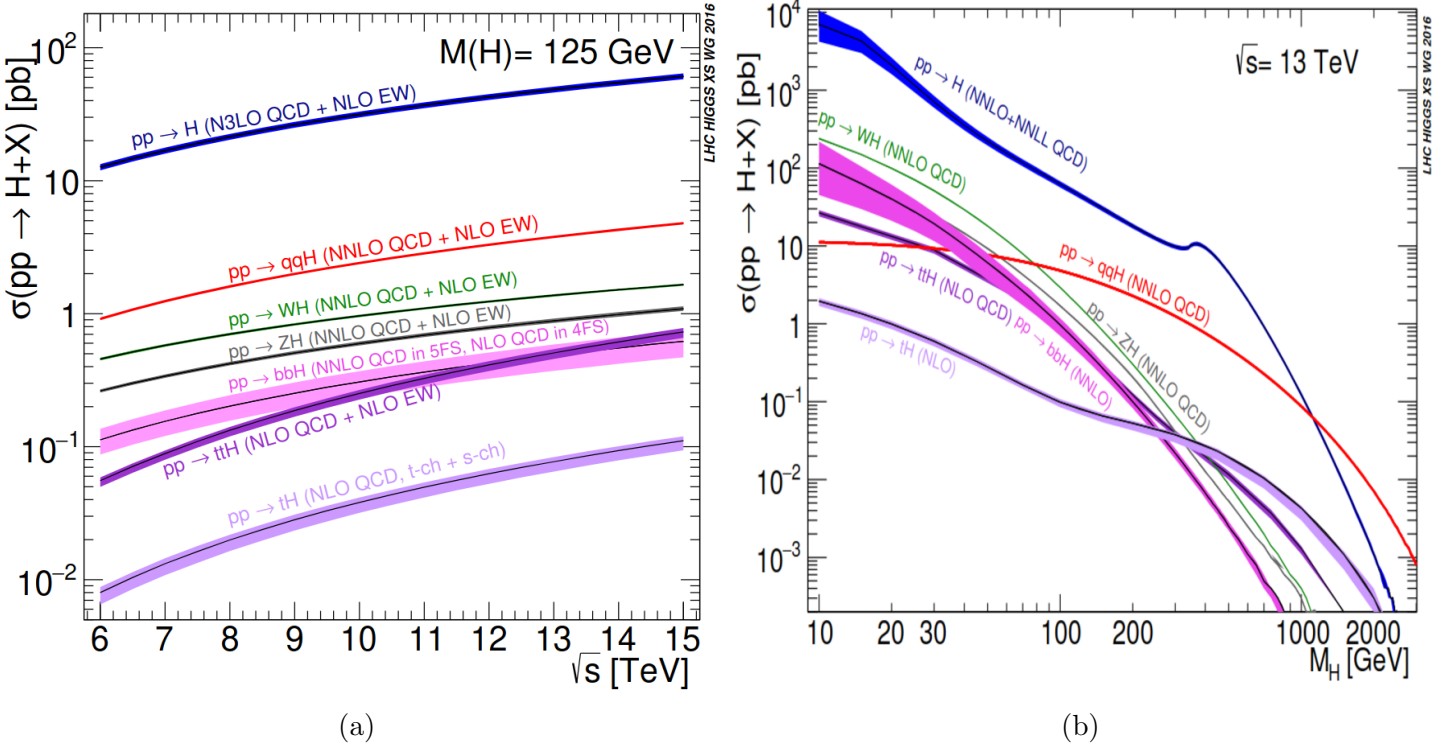


Figure 2.5: Cross sections for different Higgs boson production modes at a proton-proton collider with a centre-of-mass energy of 6-15 TeV (a). A Higgs mass of 125 GeV is assumed in this plot. Additionally, cross sections as a function of Higgs mass are shown (b) [12].

Higgs boson is an unstable particle as shown in Figure 2.6, note that the probability to decay within a given time "decay width" Γ is linked to the lifetime τ by $\Gamma\tau = \hbar$ where \hbar is the reduced Planck constant. In order to identify Higgs and its production modes, it is reconstructed from its products for a chosen decay channel.

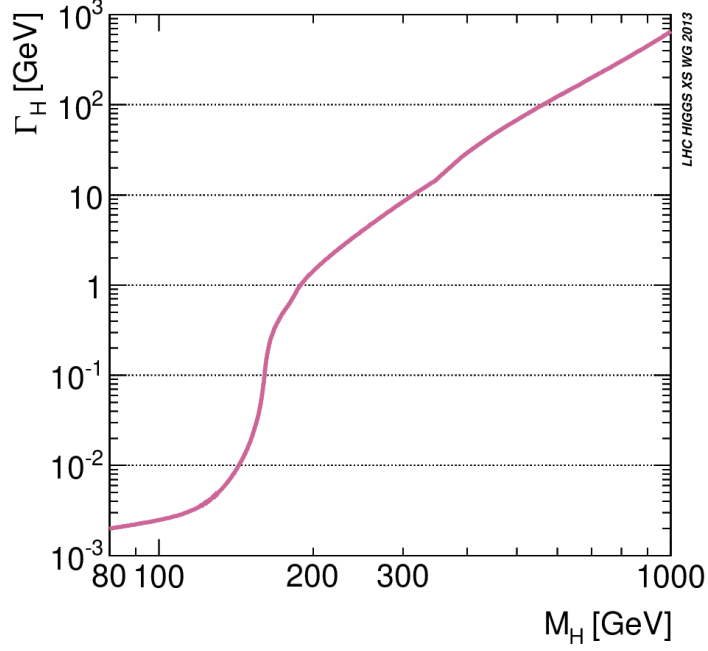


Figure 2.6: Higgs boson total decay width as a function of Higgs mass [13].

2.4.3 Higgs boson decay channels

Higgs boson decay modes and their rates.

The possible SM Higgs boson decay modes are very depend on the Higgs boson mass as shown in figure 2.7 for a Higgs boson mass range of 80 to 200 GeV. If the Higgs boson were heavy enough to decay into two real vector bosons, the modes $H \rightarrow WW^*$ and $H \rightarrow ZZ^*$ would have dominated the decay with small contribution from Higgs to di-top quarks. At very low masses of the Higgs boson, decays into vector boson or $t\bar{t}$ would have played almost no role and the dominant decay mode would have been the experimental challenging decay mode $H \rightarrow b\bar{b}$. Since photons are mass-less particles, the direct coupling

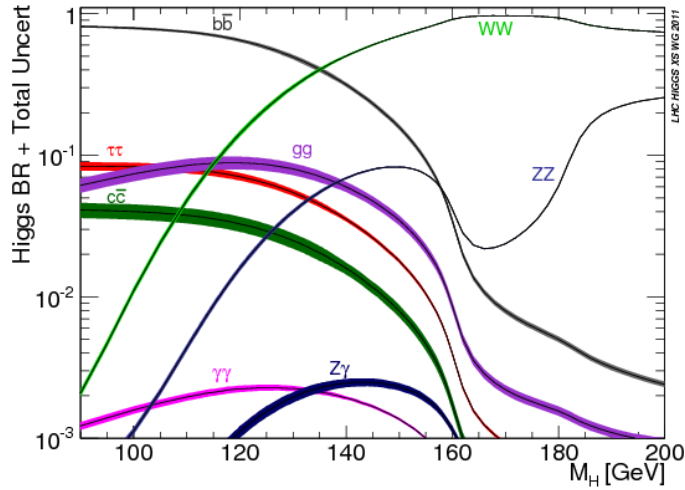


Figure 2.7: Higgs boson branching ratio of the possible Higgs decay channels as a function of the Higgs mass [14]

of the Higgs boson to photons is zero in the SM. However, the Higgs boson can decay into a pair of

photons via loop processes. The main Feynman diagrams of this decay are shown in Figure 2.8. At a Higgs boson mass of 125 GeV, the dominant decay of the Higgs boson is $H \rightarrow b\bar{b}$ with a branching ratio of roughly 58%. At the same mass $H \rightarrow \gamma\gamma$ branching ratio is around 0.23% [15].

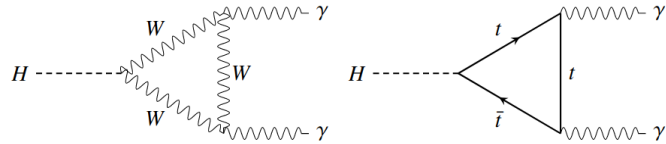


Figure 2.8: Feynman diagrams of the $H \rightarrow \gamma\gamma$ decay. Other particles can also propagate in the loop.

2.4.4 Higgs measurements

The discovery of Higgs boson in 2012 by ATLAS and CMS and first measurements of its mass. Recap of Higgs boson properties. and Introduction to self couplings no yet measured.

ATLAS and CMS collaborations, the two largest experiments of the LHC, announced on 4 July 2012 the identification with 99.99997% (5σ) of a new boson within a mass range of $125 - 127\text{GeV}$ [16, 17]. The new boson consistent the Standard Model Higgs boson properties. Later, was confirmed that the new particle, without doubt, corresponds to the Higgs boson. Higgs boson predicted in 1964, but the world had to wait until 2012 before its discovery by physicists at CERN. The Evidence of the new boson was present in the three bosonic decay modes $H \rightarrow ZZ^* \rightarrow 4l$, $H \rightarrow \gamma\gamma$ and $H \rightarrow WW^* \rightarrow l\nu l\nu$. The branching ratio of Higgs in the di-photon decay channel is small. Despite the comparably low branching fraction of this decay mode, their construction of two photons has a clean signature in the detector and allows a good energy resolution. This signal can therefore well be separated from the dominating continuum di-photon background from QCD jets, which has a smooth and well parametrisable shape. Which makes the expected Higgs boson signal significance in this decay mode is one of the highest among all the decay modes in the mass range $110 < m_H < 150\text{GeV}$. Events in data collected in 2010 and 2011 with centre-of-mass energy $\sqrt{s} = 7\text{TeV}$ and 8TeV respectively containing di-photons are combined to make the evidence of Higgs boson. Figure 2.9 shows the weighted distribution of the invariant mass of photon pairs measured by ATLAS experiments. The distributions are obtained by summing the invariant mass distributions of all of the selected events, with each event being weighted by S/B where S and B are the number of signal and background events, respectively. Figure 2.9 demonstrates a statistically significant excess of events near 125 GeV.

Measurement of the three channels are combined to confirm the observation of the new particle. The observed local significance reaches 6σ (the observed signal is $\sim 10^{-9}$ to be a background fluctuation) around 125 GeV making the first observation of Higgs boson, Figure 2.10.

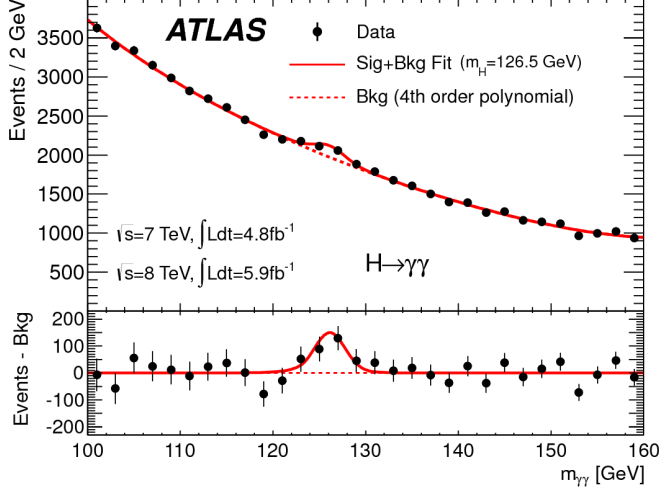


Figure 2.9: Weighted distributions of the invariant mass of di-photon [16].

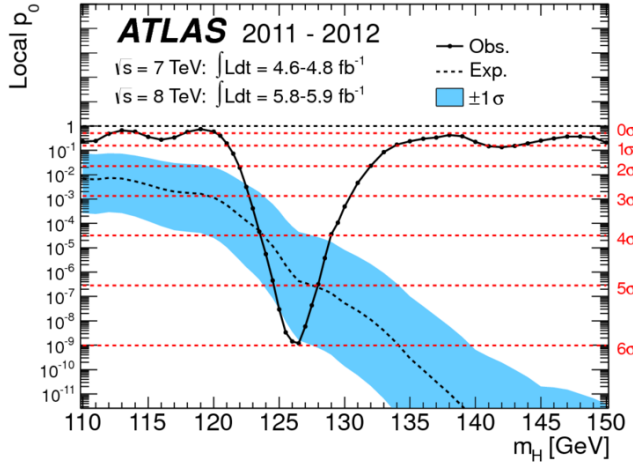


Figure 2.10: The observed local p-value as a function of m_H (solid line) and the expectation with its $\pm 1\sigma$ band assuming the presence of a Standard Model Higgs boson at that mass (dashed line) from the combination of the ZZ^* , $\gamma\gamma$ and WW^* channels by the ATLAS experiment. The horizontal dashed lines indicate the p-values corresponding to significances of 1 to 6σ [16].

The latest measurement of Higgs boson using the data collected during 2015-2018 corresponding to 139 fb^{-1} yields to a mass of $m_H = 125.09 \pm 0.24\text{ GeV}$ [18]. Figure 2.11 shows the in the di-photon invariant mass distribution. Figure 2.12 shows the best-fit values of the production cross-sections times branching fraction in different channel to the Standard Model value with the 139 fb^{-1} data.

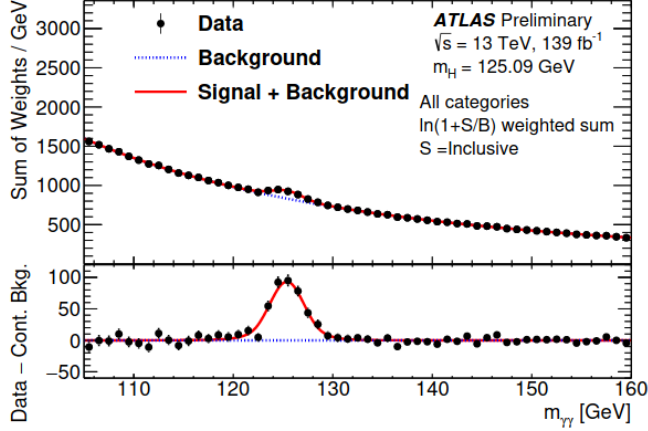


Figure 2.11: The inclusive diphoton invariant mass distribution [19].

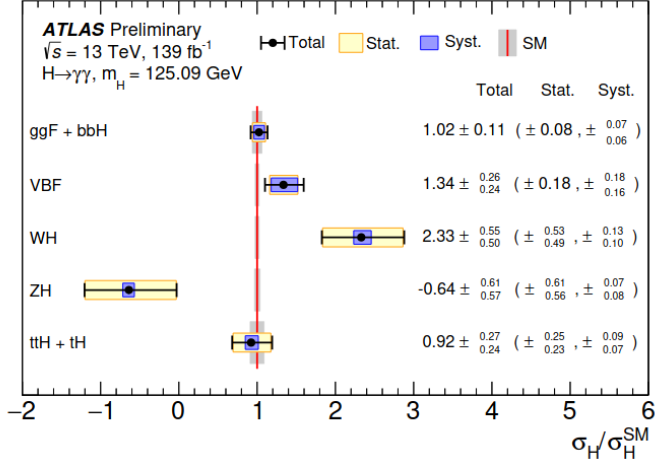


Figure 2.12: Cross sections times branching fraction for $ggF+b\bar{b}H$, VBF , VH and $t\bar{t}H+tH$ production, normalized to their SM predictions [19].

Finally, by the observation of Higgs boson the last piece of the standard model of elementary particles is founded. SM particles are summarized in Figure 2.13.

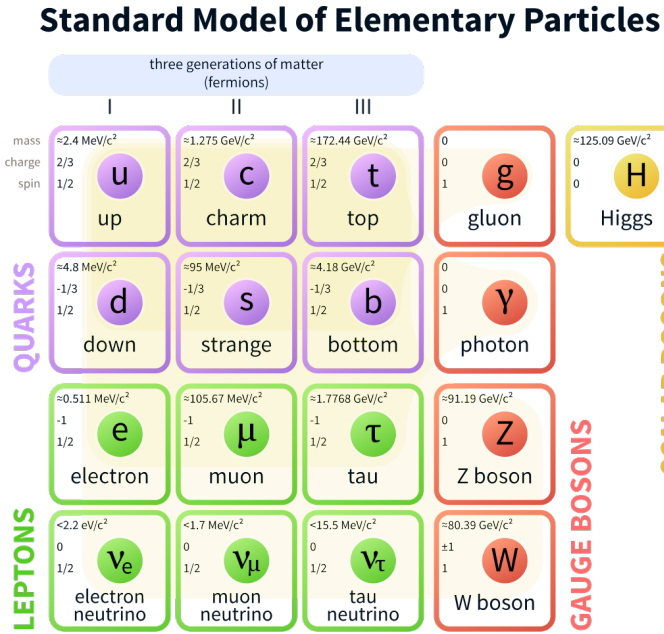


Figure 2.13: The particle content of the Standard Model (SM).

Understanding the properties and couplings of the last piece of SM is a priority of both ATLAS and CMS. Higgs self-couplings λ_{HHH} is vital, providing a direct probe on the EWSB and is a precision test of the electroweak theory. A direct probe of the trilinear coupling is possible through studying Higgs pair production where two Higgs bosons are produced in the same event, making di-Higgs analyses particularly interesting and the main subject of the thesis.

2.5 Double Higgs boson

This should contain the theory of HH and how it allows to measure the higgs self couplings.

Double Higgs production (HH) presents the only direct measurement of the Higgs self-coupling. Confirming the existence and amplitude of the Higgs Self-coupling is one of the main key prediction of the SM not observed yet. In particular, the measurement of the Higgs boson self-coupling λ (also referred to as the Higgs boson tri-linear coupling λ_{HHH}) is of great importance as expected to yield a deeper understanding of particle physics and cosmology. This measurement makes it possible to experimentally reconstruct the Higgs potential and check whether the Higgs boson discovered in 2012 at CERN is the one predicted by the Brout-Englert-Higgs mechanism. The di-Higgs production rate gives a handle to more accurately measure the Higgs potential. The main goal of this thesis is the search of Higgs boson pair production.

2.5.1 Di-Higgs production and decays

This should contain the production modes and decays of HH, and the $HH \rightarrow \gamma\gamma\bar{b}b$ channel.

As the SM provides the trilinear coupling of the Higgs boson, all SM Higgs boson production mode are known for di-Higgs production. Similarly to single Higgs boson, HH production is dominated by gluon-gluon fusion (ggF) through the destructive interference of two LO Feynman diagrams, shown in

Figure 2.14, involving top-quark loops and the triple Higgs self-coupling. In the box diagram, the top-quark Yukawa coupling λ_t is present in two vertices so the contribution of this diagram to the amplitude is proportional to λ_t^2 , while in the triangle diagram there is λ_t in one vertex and the triple Higgs self-coupling λ_{HHH} in the other vertex and the contribution of this diagram is proportional to $\lambda_t \cdot \lambda_{HHH}$. The amplitude of the process can be written as :

$$A(\lambda_t, \lambda_{HHH}) \equiv \lambda_t^2 \cdot \square + \lambda_t \cdot \lambda_{HHH} \triangle, \quad (2.24)$$

where \square represents the contribution of the box diagram and \triangle the one of the triangle diagram.

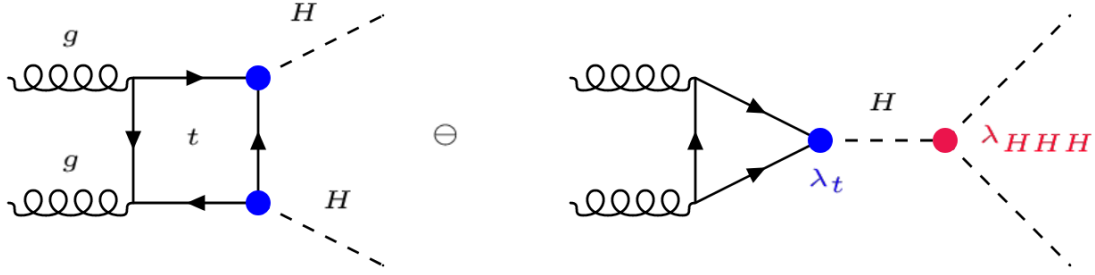


Figure 2.14: Leading Order (LO) Feynman diagrams contributing to ggF Higgs boson pair production through a top-quark loop (box) and through the triple self-coupling of the Higgs boson (triangle).

The SM cross section for Higgs boson pair production via ggF at $\sqrt{s} = 13$ TeV, calculated at Next-to-Next-to-Leading Order (NNLO) [20, 21], is:

$$\sigma_{HH}^{NNLO} = 33.53^{+4.3\%}_{-6.0\%} \text{ fb}, \quad (2.25)$$

three orders of magnitude smaller than the single Higgs production cross section. This accounts for more than 90% of the total Higgs boson pair production cross section. VBF mode also contribute to the di-Higgs production with a very low cross section (two orders of magnitude smaller). Therefore only the ggF production mode is considered in this thesis. Figure 2.16 shows the other production modes contributing to Higgs pair production. The corresponding cross section as a function of centre-of-mass energy is shown Figure 2.15.

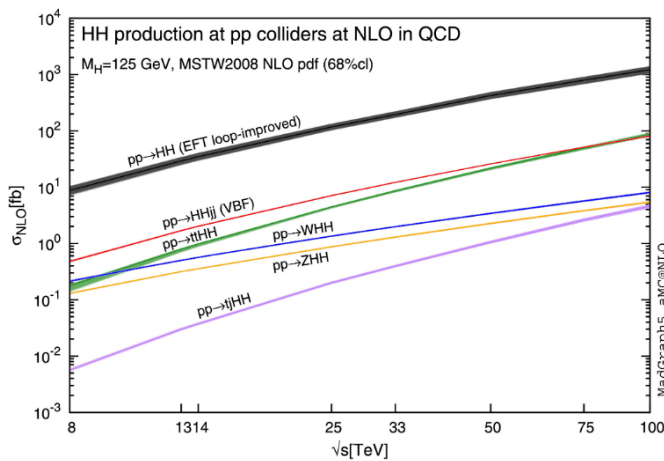


Figure 2.15: Total cross sections at the NLO for HH production as a function of centre-of-mass energy. Assuming κ_λ and κ_t equals to their SM values.

Figure 2.17 presents the matrix of the decay channels of Higgs boson pair resulting from all possible combination of decays of the two Higgs bosons. The dominants channels are $HH \rightarrow b\bar{b}b\bar{b}$, $HH \rightarrow b\bar{b}\tau\tau$ and $HH \rightarrow b\bar{b}WW^*$.

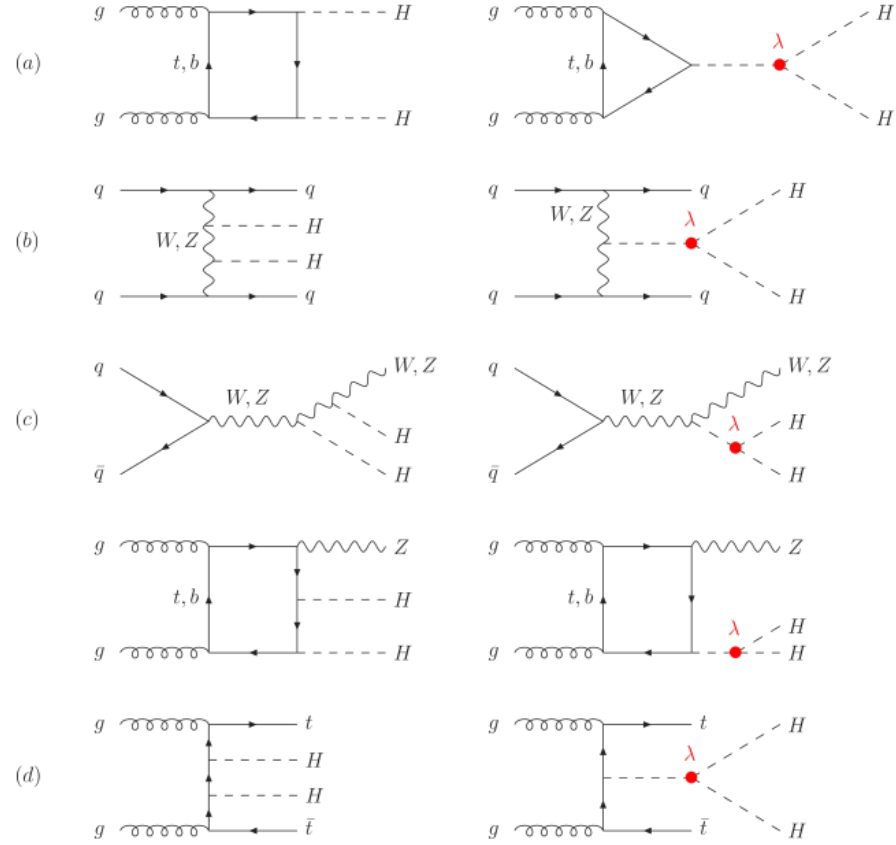


Figure 2.16: HH production modes, in decreasing order of cross section. λ referees to Higgs tri-linear coupling: (a) ggF mode, (b) VBF mode, (c) Vector boson association (VH) and (d) top associated production.

	bb	WW	$\tau\tau$	ZZ	$\gamma\gamma$
bb	33%				
WW	25%	4.6%			
$\tau\tau$	7.4%	2.5%	0.39%		
ZZ	3.1%	1.2%	0.34%	0.076%	
$\gamma\gamma$	0.26%	0.10%	0.029%	0.013%	0.0005%

Figure 2.17: Di-Higgs system decay branching ratios assuming SM Higgs bosons with $m_H = 125.09$ GeV.

Even if there are other channels with branching ratios higher by one or two orders of magnitude, $b\bar{b}\gamma\gamma$ final state is one of the most promising decay channels for the search for di-Higgs production as it has a good compromise between the very large branching ratio from $H \rightarrow b\bar{b}$ decay and the small Higgs to diphoton branching ratio. The $\gamma\gamma b\bar{b}$ channel is appealing thanks to an excellent diphoton resolution leads on a clean di-photon signature giving a narrow peak at Higgs mass in the $m_{\gamma\gamma}$ invariant mass spectrum on top of a smoothly falling background. These helps in separating the signal from the background processes. This thesis is preformed on $\gamma\gamma b\bar{b}$ final state.

2.5.2 Di-Higgs as a probe of BSM physics

How κ_λ cloud probe the existence of BSM effects

The small cross section (Eq. 2.25) is challenging to measure. If SM expectations hold, the production of a Higgs boson pair in a single pp interaction should not be observable with the currently available LHC data set, unless its cross section is enhanced by an anomalous (new physics). Which makes HH production a promising process to probe new physics beyond the standard model (BSM). Beyond the Standard-Model (BSM) scenarios may enhance the Higgs boson pair production rate and would be indicating a new physics. Many of those BSM theories predict the existence of heavy particles that can decay into a pair of Higgs bosons. These could be identified as a resonance in the di-Higgs invariant mass spectrum. In addition to the resonant production, there can also be non-resonant enhancements to the Higgs boson pair cross section. Only the non-resonance search is considered in this thesis. These can either originate from loop corrections involving new particles, such a light colored scalars, or through non-SM couplings. Anomalous couplings of Higgs boson with the top-quark or triple Higgs self-coupling can either be extensions to the SM, such as contact interactions between two top quarks and two Higgs bosons, or be deviation from the SM values of the trilinear Higgs coupling. Considering possible modifications of them, the deviation is quantified by $\kappa_\lambda = \frac{\lambda_{HHH}}{\lambda_{HHH}^{SM}}$ and $\kappa_t = \frac{\lambda_t}{\lambda_t^{SM}}$, where λ_i is the coupling i of the new physics and λ_i^{SM} its SM value.

Given the κ_t and κ_λ modifiers, the Higgs pair production cross section can be parameterised as :

$$\sigma \approx k_t^4 \left[|\square|^2 + \frac{k_\lambda}{k_t} (\square \triangle + \triangle \square) + \left(\frac{k_\lambda}{k_t} \right)^2 |\triangle|^2 \right], \quad (2.26)$$

this shows that the production cross section depends on both parameters κ_t and κ_λ , while the kinematics only depends on their ratio, that modifies the relative contribution of the two diagrams and thus the shape of the kinematic distributions. The maximum interference between the two diagrams corresponds to the cross section minimum located at $\kappa_\lambda = 2.4\kappa_t$. Figure 2.18 shows an illustration of diagram contribution to the invariant mass distribution of di-Higgs system m_{HH} . The box diagram has an invariant mass spectrum peaking around $2m_t$. When including the triangle diagram with the triple Higgs self-coupling, the invariant mass spectrum becomes generally softer with the increase of its contribution. This effect cause a large change in m_{HH} distribution as shown in Figure 2.19.

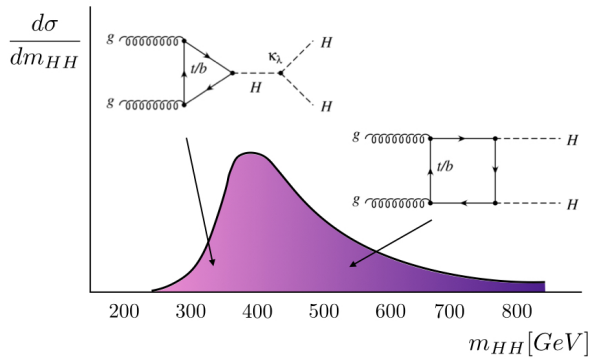


Figure 2.18: Illustration of both box and triangle diagrams contribution to di-Higgs invariant mass spectrum.

The interference of the two diagrams also generates local minima in the differential cross section around $m_{HH} = 2m_t$ for the case of $\kappa_\lambda = 2$.

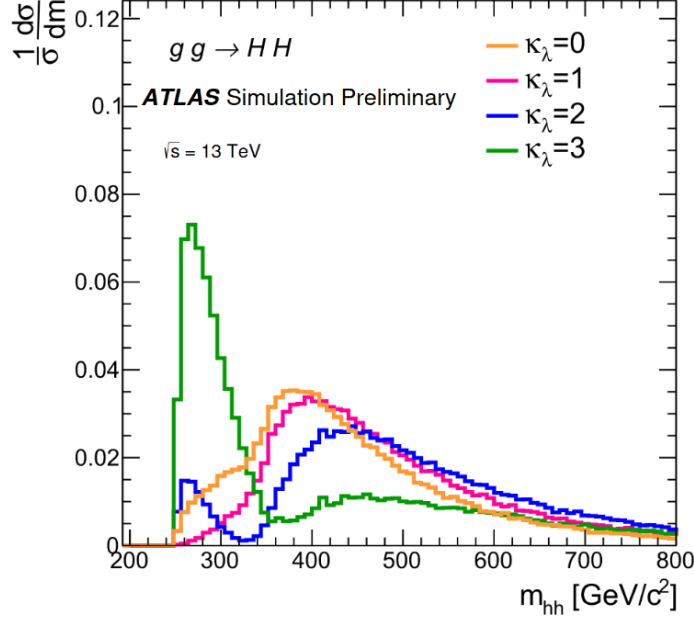


Figure 2.19: Higgs pair invariant-mass distribution in ggF for various values of κ_λ assuming $\kappa_t = 1$.

Figure 2.20 displays total LO and NLO cross sections for the six dominant HH production channels at the LHC with $\sqrt{s} = 14$ TeV, as a function of the self-interaction coupling κ_λ . The SM value of the cross section corresponds to $\kappa_\lambda = 1$. As mentioned above, Higgs pair production is a promising process to probe new BSM physics. In this thesis, in addition to searching for the SM Higgs pair production process, constrain on κ_λ is also extracted.

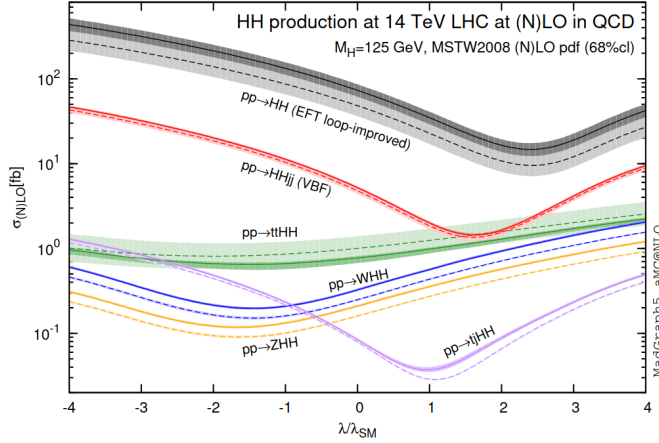


Figure 2.20: Total LO and NLO cross sections for HH production at the LHC with $\sqrt{s} = 14$ TeV, as a function of the self-interaction coupling κ_λ .

2.5.3 Current Measurements

This includes the 36 fb^{-1} results and the limit on HH cross section and κ_λ .

At the beginning of this thesis (2018), the latest measurement of Higgs pair production in $HH \rightarrow \gamma\gamma\bar{b}b$ channel was preformed with an amount of data of 36.1 fb^{-1} representing the data collected by ATLAS

detector in 2015 and 2016 (Chapter 3 is dedicated to ATLAS detector). Results of the previous analysis were consistent with the SM expectations [22]. In the non-resonant case, results are interpreted in the context of κ_λ . The analysis set an observed (expected) 95% CL upper limit on HH cross section of 0.73 (0.93) pb, corresponding to 22 (28) times the predicted SM value. The Higgs self coupling is constrained to be between $-8.2 < \kappa_\lambda < 13.2$ at 95% CL ($-8.3 < \kappa_\lambda < 13.2$ expected), other SM parameters are fixed to their expected value when extracting limits. The limit scan of κ_λ is shown in Figure 2.21.

Contributing to the $HH \rightarrow \gamma\gamma b\bar{b}$ non-resonant analysis involves 139fb^{-1} of data collected during the Run 2 (2015-2018) of the LHC program, and improve the current limits on the cross-section and self-coupling is the aim of this thesis.

	Observed	Expected	-1σ	$+1\sigma$
$\sigma_{gg \rightarrow HH} [\text{pb}]$	0.73	0.93	0.66	1.3
As a multiple of σ_{SM}	22	28	20	40

Table 2.2: The 95% CL observed and expected limits on the Higgs boson pair cross-section in pb and as a multiple of the SM production cross-section. The $\pm 1\sigma$ band around each 95% CL limit is also indicated.

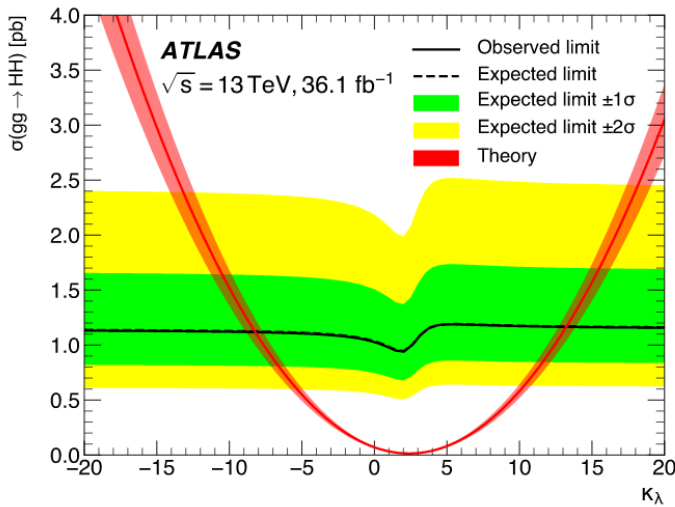


Figure 2.21: The expected and observed 95% CL limits on the non-resonant production cross section $\sigma_{gg \rightarrow HH}$ as a function of κ_λ . The red line indicates the predicted HH cross section if κ_λ is varied but all other couplings remain at their SM values. The red band indicates the theoretical uncertainty of this prediction.

2.6 Effective Field Theory (EFT)

A brief introduction to EFT and how it helps to probe physics at large scale.

In the context of search for BSM physics, so far, no indication has been found at the LHC. This could be explained by the fact that the new physics is not accessible at the LHC. Effective Field Theories (EFTs) provide an approach to probe the existence of BSM physics in a model independent way at the LHC, even if the new physics scale Λ is not directly accessible at the LHC. When BSM resides at scales larger than the EW scale ($\Lambda >> vev$), the new physics decouples from the SM and no light hidden states are

produced. When this condition is satisfied, an expansion of the Lagrangian is canonical dimensions of $\frac{vev}{\lambda}$ can be performed. The theory that results is the Standard Model Effective Field Theory (SMEFT) [23]. The SMEFT is well defined and has been studied with increased theoretical sophistication in recent years, and it can capture a wide range of possible extensions of the SM. Such SM extensions can address the strong evidence for dark matter and neutrino masses not covered by SM. A linear EFT model of SMEFT is considered in this thesis :

$$\mathcal{L}_{SMEFT} = \mathcal{L}_{SM} + \mathcal{L}^5 + \mathcal{L}^6 + \mathcal{L}^7 + \dots, \quad \mathcal{L}^d = \sum_{i=1}^{n_d} \frac{C_i^d}{\Lambda^{d-4}} Q_i^d \quad \text{for } d > 4. \quad (2.27)$$

The number of non-redundant operators in \mathcal{L}^i is known. The operators Q_i^d are suppressed by $d-4$ powers of the cutoff scale Λ . These operators build a complete set of all operators allowed by the SM gauge symmetries. The Warsaw basis is used for the invariant operators Q_i^d [24]. The coefficients C_i^d are called Wilson coefficients. They are free parameters of the theory.

The new physics interferes with the standard model, and modify the kinematics of the given process. The cross section of a specific process within the SMEFT can be splitted as :

$$\sigma = \sigma_{SM} + \sigma_{int} + \sigma_{BSM}, \quad (2.28)$$

where σ_{SM} is the SM cross section, σ_{int} represents the interference between the BSM physics with the SM, and σ_{BSM} is a pure BSM physics suppressed by Λ^{-4} that does not depend on the SM amplitude; it can however become important in specific regions of the phase space and its consideration can prevent negative cross sections.

Projecting measurements of the interactions of the known Standard Model (SM) states into an effective field theory (EFT) framework is an important goal of the LHC physics program [25]. The interpretation of measurements of the properties of the Higgs boson in an EFT allows one to consistently study the properties of this state. Similarly to κ_λ variations, new physics can affect Higgs pair production. Higgs pair production results can benefit from an interpretation beyond the κ_λ variations. The full Run 2 di-Higgs results can be used to set limits on SMEFT parameters. Detailed studies of EFT within double Higgs context are described in the dedicated Chapter **To Be Added**.

2.7 Conclusion

Brief conclusion of chapter 1.

Higgs mechanism was introduced into the SM to explain the origin of the masses of the particles. A particle with similar proprieties to SM Higgs boson was discovered at collisions of LHC in 2012. After its discovery, a priority of the ATLAS and CMS collaborations has been to better understand its properties and couplings. Understanding Higgs self-coupling is vital providing a direct probe on electroweak symmetry breaking (EWSB) and reconstruct the Higgs potential to check whether the boson discovered is Higgs boson. The theoretical backgrounds needed to understand the main subject of the thesis are introduced. As well as the current results with 2015-2016 data. The EFT is highlighted as an interpretation of di-Higgs results beyond κ_λ . Next chapter focus on the experimental setup to produce and collect data, the Large Hadron Collider and the ATLAS detector.

The Large Hadron Collider and the ATLAS detector

This chapter will include :

- LHC description and how it works
- different LHC points
- focus on ATLAS as main experiment
- focus on EM and H calorimeters

Copy past from other thesis!

The physics described in this thesis exclusively uses data collected by the ATLAS (A Toroidal LHC Apparatus) detector raised from high-energy proton-proton collisions, accelerated by the Large Hadron Collider (LHC). In terms of achievable centre-of-mass energy, LHC is currently the most powerful particle accelerator on Earth. The structure, parameters and principles of LHC and ATLAS, besides the complex sub-detecting system introduced in this chapter.

3.1 The Large Hadron Collider

LHC is a circular accelerator of hadrons with a circumference of 27 kilometers. It was designed to accelerate and collide proton beams with a centre-of-mass energy up to 14 TeV as well as heavy ions, in particular lead nuclei (Pb), at 2.3 TeV per nucleon. Inside this circular accelerator a set of protons (or nucleons) so-called bunch racing clockwise at near the speed of light (99.9999991%) crashes into an other bunch speeding anticlockwise. The energy involved in the collisions is so great that, in a sub-microscopic region at the heart of the collisions, it briefly generates conditions similar to those that occurred shortly after the birth of the Universe. This machine is installed in the 27 km tunnel, located underground between 50 m and 175 m depth, that was built between 1984 and 1989 for the LEP e^+e^- machine. In 2001, LEP was dismounted to give way to the LHC.

Within the tunnel are two adjacent parallel beam pipes and surrounded by superconductive magnets. In total there are 1232 dipole magnets which bend the beams into its circular orbit and 392 quadrupole magnets corresponding to the function of beams focusing. The strength of the focusing magnets is required to be high to squeeze the transverse beam sizes and, thus, increase the chances of collisions. The adopted design at the LHC is approximately 80% of the arcs is filled with dipole magnets. Dipoles are also equipped with sextupoles, octupoles and decapoles, function of which is to correct non-linear dynamics of the beams. Keeping 7 TeV proton energy beam on the designed orbit implies the use of

magnetic bending fields of 8.4 T. Generation of such field requires to use superconducting magnets at the limit of the existing technologies. Approximately 96 tonnes of liquid helium is needed to maintain the superconductivity of the magnets at operational temperature of 1.9 K (-271.3C), making the LHC the largest cryogenic facility in the world. A detailed description of the LHC and the CERN accelerator complex is given in Ref. [26].

3.1.1 Acceleration chain

A succession of small to large accelerators is used to accelerate the protons extracted from Hydrogen gas to the energy needed for injection into the LHC. Figure 3.1 shows the CERN accelerator complex including all pre-acceleration steps before the LHC. The process of the acceleration starts from the linear

CERN's Accelerator Complex

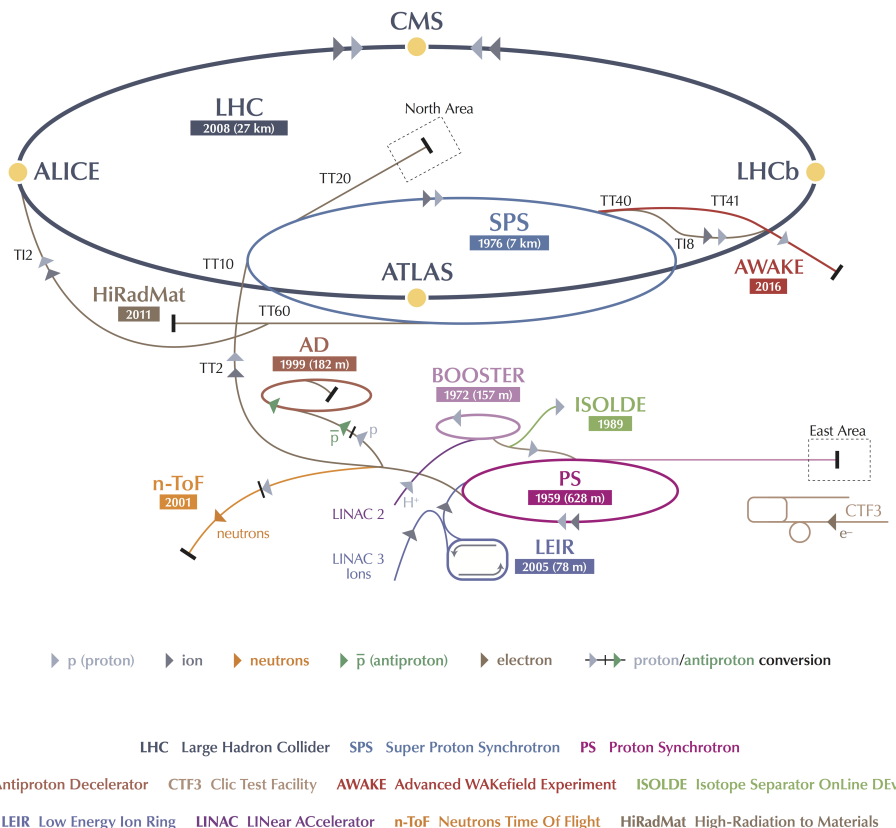


Figure 3.1: Overview of the CERN accelerator complex, including the LHC and its pre-accelerators [27]. The four main LHC experiments are depicted, too

accelerator Linac 2, which accelerates the protons up to 50 MeV. The beam is then injected into the Booster. The Booster accelerates the protons to 1.4 GeV and feeds the Proton Synchrotron (PS), where the protons are further accelerated to 25 GeV. The next chain is the Super Proton Synchrotron (SPS), which is 6.9 km long. Here the protons reach the energy of 450 GeV before they are transferred to two beam-pipes of the LHC main ring. The beams are injected in bunches contained $\sim 10^{11}$ protons each. Beams contain ~ 2808 bunches spaced by 25 ns with transverse dimension of the order a millimeter.

3.1.2 Luminosity

The number of collected events is proportional to the luminosity multiplied by the cross section:

$$N_{events} = \int \mathcal{L} dt \times \sigma_{process}. \quad (3.1)$$

The luminosity is the quality factor for colliders, measuring the intensity of the beam, luminosity is defined as :

$$\mathcal{L} = \frac{N_b^2 n_b f_r \gamma_r}{4\pi \epsilon_n \beta^*} F, \quad (3.2)$$

where for the design luminosity (nominal parameters for the LHC are given in parenthesis):

- N_b is the numbers of particle per bunch ($\sim 10^{11}$).
- n_b is the number of bunch per beam (2808).
- f_r is the revolution frequency (11245 Hz).
- γ_r is the relativistic γ factor (~ 700).
- ϵ_n is the normalized traverse beam emittance-characterizes its spread in coordinate and momentum phase space (3.75 μm).
- β^* is the beta function at the collision point determined by the magnets configuration (for ATLAS 0.55m).
- F is the geometric luminosity reduction factor due to the crossing angle at the interaction point.

In ATLAS, we have define a basic time unit called a Luminosity Block (LB) where the luminosity is assumed to be stable inside each LB. The typical LB duration is one to two minute. Data are analyzed under the assumption that each LB contains data taken under uniform conditions (data quality). To define a data sample for physics, quality criteria are applied to select LBs where condition are acceptable, then the average luminosity in that LB is multiplied by the LB duration to provide the integrated luminosity delivered in that LB.

The design luminosity of LHC is $10^{34} \text{cm}^{-2}\text{s}^{-1}$. The Figure 3.2 shows the delivered and recorded luminosity during the Run 2 data taking [28]. Only $\mathcal{L}_{int} = 139 \text{fb}^{-1}$ is used for physics since small fraction of full Run 2 data does not pass the good quality criteria. The analyse described in this thesis is performed on the 2015-2018 data subsets.

Knowing the cross section of the $HH \rightarrow \gamma\gamma\bar{b}b$ production, one can evaluate the number of events available for the analysis as $N_{HH \rightarrow \gamma\gamma\bar{b}b} = \mathcal{L}_{int} \cdot \sigma_{pp \rightarrow HH} \cdot Br(HH \rightarrow \gamma\gamma\bar{b}b)$ that leads to about 12 events.

3.1.3 Pile-up

Because of the very high density of protons at the collision points, more than one proton interact when two LHC bunches cross each other at the center of the experiment. This is commonly referred to as pileup. On top of the usual *in – time* pileup, defined as the collision events occurring during the same bunch-crossing as the event of interest, one also has to consider *out – of – time* pileup, coming from remnants of information found in some of the detector subsystems that end-up being attributed to the wrong bunch-crossing, and therefore to the wrong event typically from previous collisions. Figure 3.3

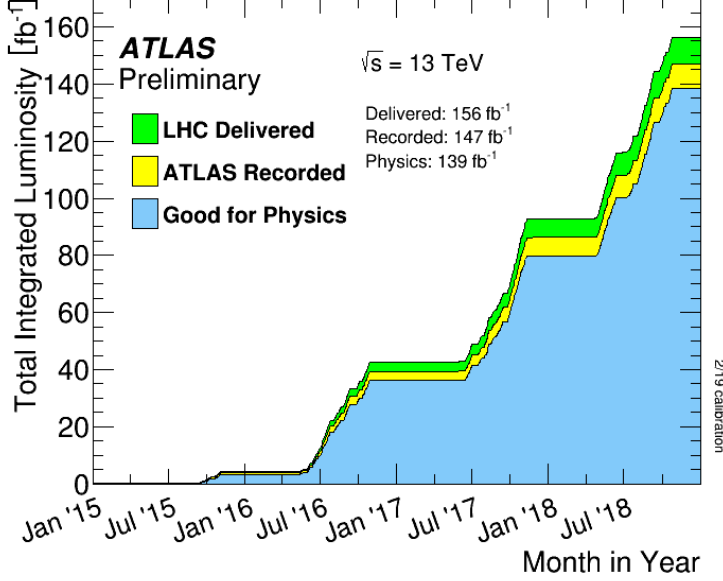


Figure 3.2: Luminosity delivered by the LHC during the Run 2 data taking. ATLAS recorded this data with an efficiency above 90%.

shows the average number of simultaneous interactions per bunch crossing for Run 2.

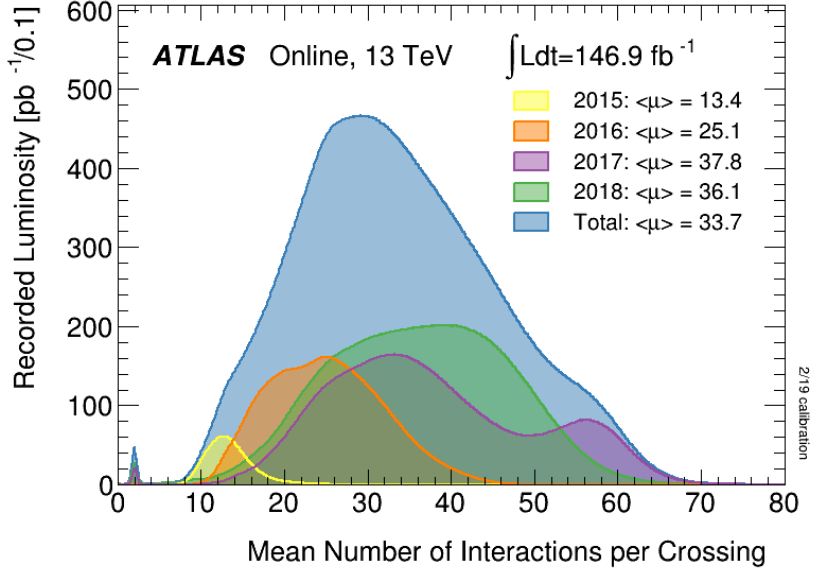


Figure 3.3: Mean number of interaction per bunch crossing in pp collisions recorded by the ATLAS detector during Run 2 at 13 TeV [28].

The particles created in LHC collisions are distributed over the full solid angles around the Interaction Point (IP), in four IP point is installed four detectors to record those particles and identified them as ATLAS, CMS, ALICE and LHCb each is specific to study a category of physics. LHCb built to study flavour physics looking at the properties of b-hadrons, and the ALICE detector that is specialised for measurements on heavy-ion collisions. CMS and ATLAS are general-purpose detectors. They allow

to make precision measurements of SM processes, including the properties of the Higgs boson, and to search for physics beyond the SM. Next section is dedicated to ATLAS detector as the thesis is done withing ATLAS collaboration.

3.2 ATLAS A Toroidal LHC ApparatuS detector

ATLAS detector is one of the four experiments placed on the four crossing points of the LHC beams. It is currently the largest experiment of particles 46 m long and 25 m of diameter and more than 7000 tons of weight [29]. It is a superposition of four sub-detectors, each optimized for the identification and the measurement of a specific category of particles : Inner Tracker, Electromagnetic Calorimeter (ECAL), Hadronic Calorimeter (HCAL) and Muons Spectrometer. It is composed of central called Barrel and two End-Cap to cover the 4π solid angle. The detector has been operating since 2008, taking alignment data with cosmic rays before the LHC launch, and its data is exploited by a collaboration of about 3000 scientific authors from 181 institutions in 38 countries. An overview sketch of the ATLAS detector is shown in Figure 3.4.

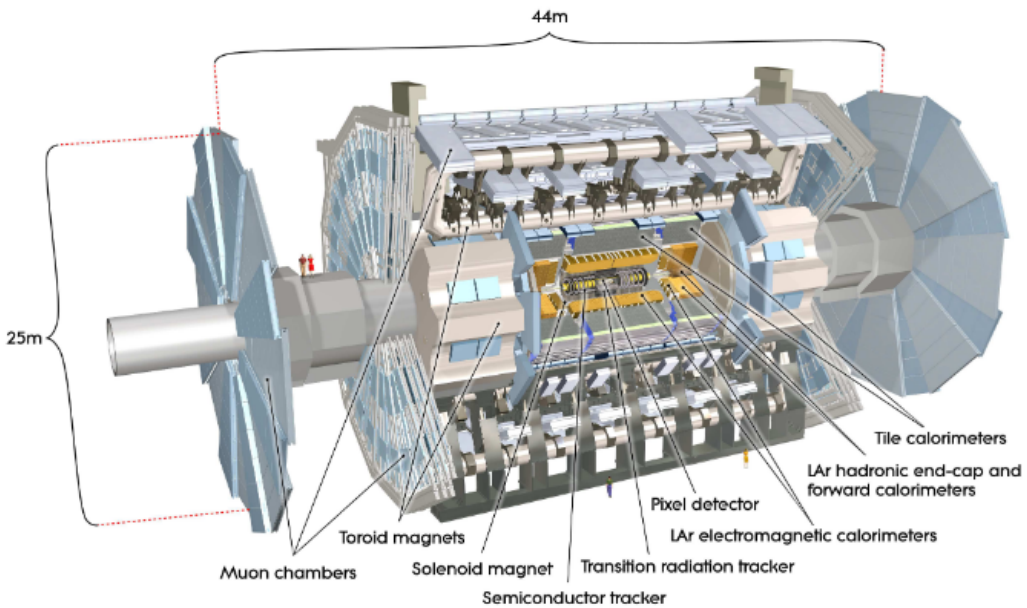


Figure 3.4: Sketch of the ATLAS detector with its different sub-detectors.

3.2.1 Coordinated system

The coordinate system used in the ATLAS experiment is cylindrical coordinates with the z-axis is the LHC beam pipe, the x-axis pointing toward the center of the LHC ring and the y-axis pointing upward. A physic object (particle) is identified by its transverse competent of the three-momentum $p_T = \sqrt{p_X^2 + p_Y^2}$, its azimuthal angle $\phi \in [-\pi, \pi]$ formed by the three-momentum and the x-axis and its polar angle $\theta \in [0, \pi]$, i.e the angle between the three-momentum and the z-axis.

The polar angle is expressed in terms of the pseudo-rapidity η , defined as

$$\eta = -\log[\tan(\theta/2)]. \quad (3.3)$$

In protons collisions, the adoption of η instead of θ ensure the detector balance over particles and particles distribution recorded is approximately flat with respect to η .

$$\frac{\partial\sigma_{QCD}}{\partial\eta} = cte. \quad (3.4)$$

The pseudo-rapidity η coincides for relativistic particles to the rapidity y , defined as

$$y = \frac{1}{2} \left(\frac{E + p_z}{E - p_z} \right), \quad (3.5)$$

where E is the particle energy. Figure 3.5 shows the coordinate system common by ATLAS and CMS experiments.

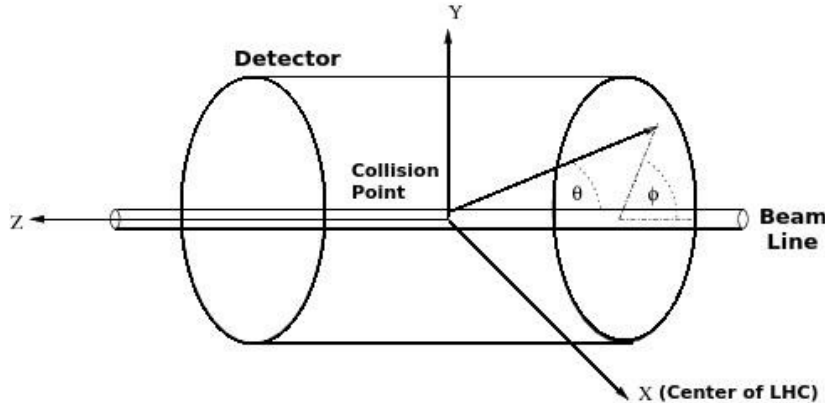


Figure 3.5: Coordinate system used by the ATLAS and CMS experiments at the LHC.

3.2.2 The Inner Tracker

The Inner Detector (ID) has been designed to detect and reconstruct the path of the electrically charged particle bent by a 2T solenoid magnetic field, and provides an excellent momentum resolution by reconstructing curvature and direction, and both primary and secondary vertex measurements for tracks above approximately 0.5 GeV[30, 31]. In terms of acceptance, the ID cover region of $|\eta| \leq 2.5$. To achieve the momentum and vertex resolution requirements imposed by the physics goals at the LHC and the very large track density environment, the ID high-precision measurements must be made with fine detector granularity. The ID is composed of four complementary sub-detectors: IBL, the Pixel Detector, the Semi Conductor Tracker (SCT) and the Transition Radiation (TRT). The magnetic field of 2 T is provided by a solenoid inserted between the ID and the EM calorimeter. The layout of the Inner Detector (ID) is illustrated in Figure 3.6.

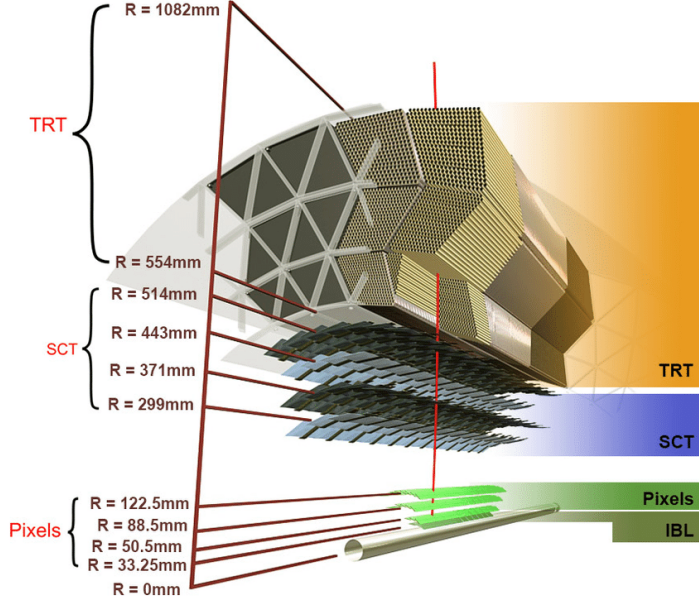


Figure 3.6: Layout of the Inner Detector (ID), including the new Insertable B-Layer (IBL) [32].

IBL

In 2014, at the first LHC long shutdown, the ATLAS pixel detector was complete with a pixel layer installed close to the beam pipe called Insertable B-Layer (IBL) [33]. It means motivations are :

- Insure the good identification of the primary vertex which play an important role in b -jet identification (b -tagging), which in turn significantly improves the sensitivity of many analyses. Inefficiencies in the other layers can be partially compensated during reconstruction at the cost of an increased fake rate, the IBL restore the full b -tagging efficiency even in case of a complete B-layer failure.
- Luminosity effects, The current pixel detector was designed for a peak luminosity of $10^{34} \text{ cm}^{-2} \text{ s}^{-1}$. With high luminosity the event pileup is increased, leading to high occupancy that can induce readout inefficiencies, would thereby limit the b -tagging efficiency. The addition of the IBL layer helps to preserve tracking performance in face of luminosity effects.

Strong constraints and project specifications have a substantial impact on the technologies required for the IBL. IBL covers the region of $|\eta| < 2.58$ in pseudo-rapidity and located at a mean radius of 33.2 mm around the beam pipe. The pixels uses 12 million pixels with a typical size of $50 \times 250 \mu\text{m}$. The IBL consists of 14 staves with each 20 modules made using either planar or 3D sensors. The temperature of the IBL is controlled using a bi-phase CO₂ cooling system. Figure 3.7 shows the IBL within the Pixel Detector volume and around the beam pipe.

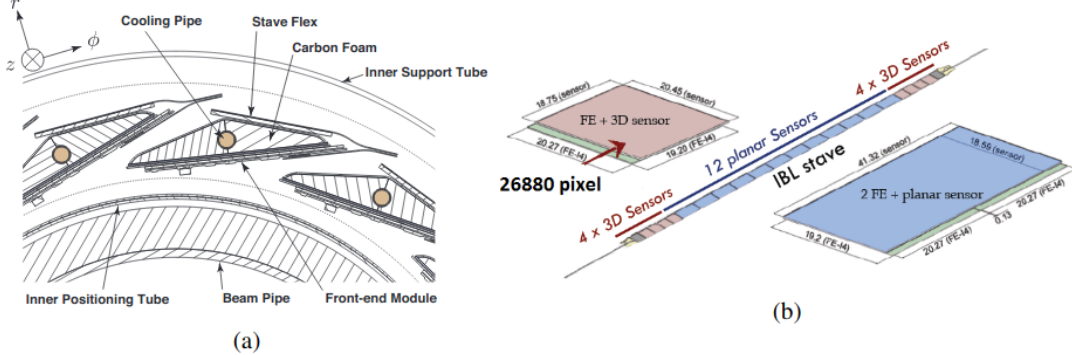


Figure 3.7: (a) Transverse view of 3 of the Insertable-B-Layer (IBL) staves, located directly on the beam pipe. (b) The layout of one of the 14 IBL staves [32].

Additional measurement point provided by IBL improves significantly the tracking. Figure 3.8 shows the improvement in impact parameter resolution due to the IBL as measured from early Run 2 data with respect to Run 1.

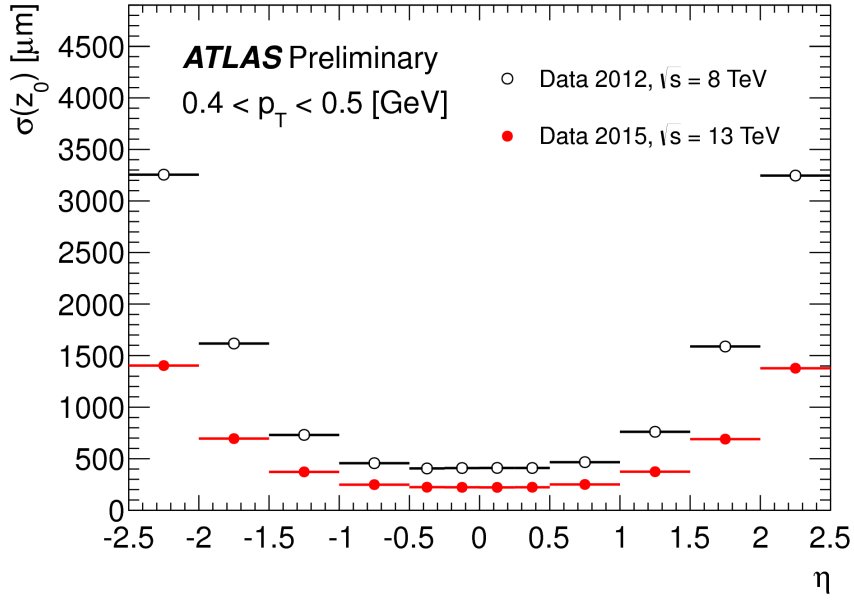


Figure 3.8: Unfolded longitudinal impact parameter resolution measured from data in 2015, $\sqrt{s} = 13 \text{ TeV}$, with the Inner Detector including the IBL, as a function of η for values of $0.4 < p_T < 0.5 \text{ GeV}$ compared to that measured from data in 2012, $\sqrt{s} = 8 \text{ TeV}$ [34].

In addition to a factor of 4 reduction in reconstruction times [35], Figure 3.9 shows the improvement achieved with IBL for the performance of tracking in dense environments (TIDE). Improvements in tracking have a direct impact on vertex identification and b -tagging.

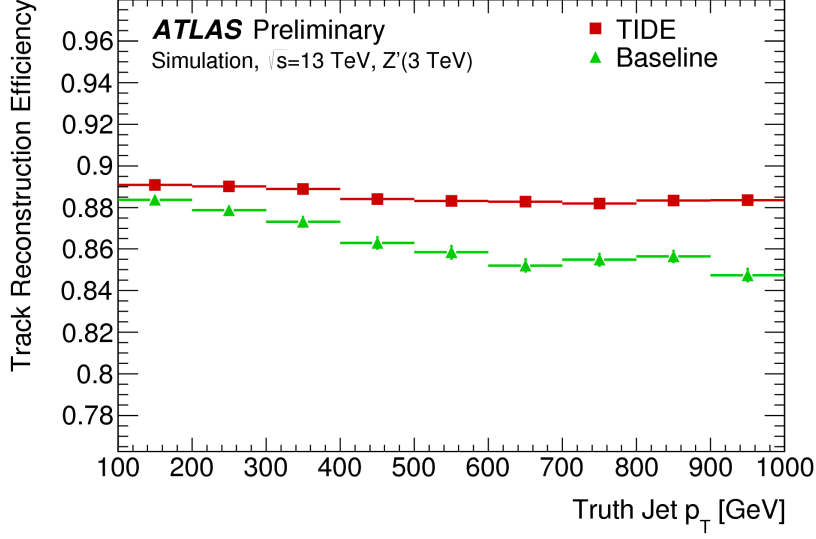


Figure 3.9: The average efficiency to reconstruct primary tracks with a production vertex before the first layer in jets as a function of jet p_T . The same sample generation, with limited statistics, is used for both reconstruction algorithms resulting in correlated features [36].

Figure 3.10 shows the improvement in the b -tagging efficiency with IP3D+SV1 b -tagging algorithms respect to Run 1 algorithm due to the IBL [37, 38]. The IP3D and SV1 algorithms will be explained later in the thesis.

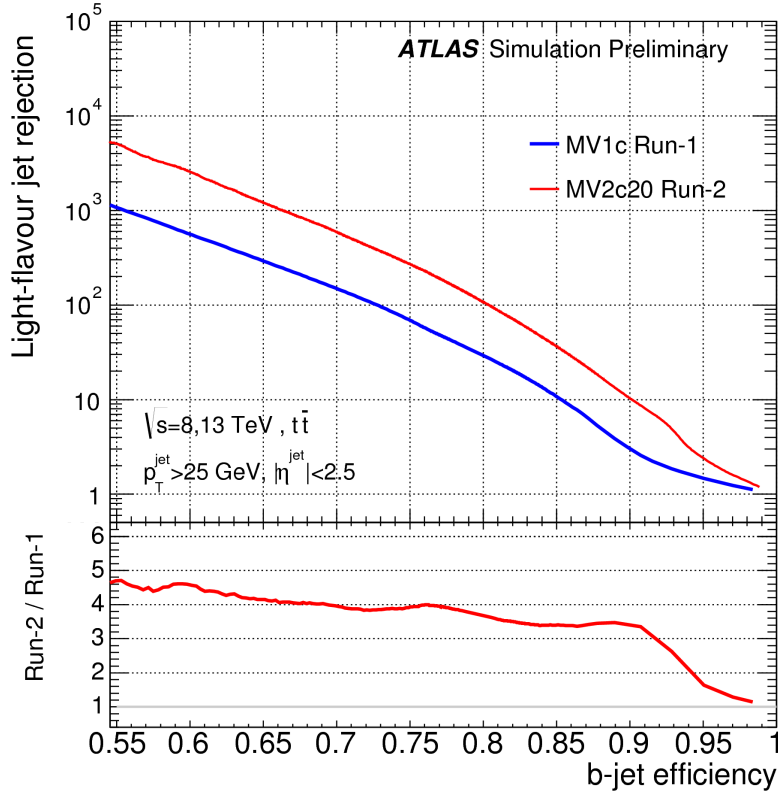


Figure 3.10: Rejection factor against light jets as a function of b -jet efficiency for the combined IP3D+SV1 tagger. Compared are the results with and without IBL.

Pixel Detector

The Pixel Detector (PD) is designed to provide high-granularity, high-precision measurements as close as possible to the interaction point (IP). It consists of three barrel layers placed at the radius of 50.5 mm , 88.5 mm and 122.5 mm centered around the beam axis and two end-cap with three disc layers each positioned at $|z| = 495.580$ and 650 mm . It provides three measurement points per track. The system is designed to be highly modular, containing approximately 1500 identical barrel modules and 1000 identical disk modules, each module is composed of 61440 pixel elements of silicon semi-conductor. In total there are about 80 million readout channels in the whole PD. The spatial resolution for the barrel modules is $10\text{ }\mu\text{m}$ in $r\text{-}\phi$ and $66\text{ }\mu\text{m}$ in z , for the end-caps the spatial resolution in $r\text{-}\phi$ is same as the barrel and $115\mu\text{m}$ in r . The main limitation of the pixel detector is the radiation hardness as the expected flounce is at the tolerable limit.

Semi Conductor Tracker

The SCT system is designed to provide four precision points per track in the intermediate radial range, contributing to the measurement of momentum, impact parameter and vertex position. The barrel and end-caps SCT are four layers of silicon microstrip for barrel and nine disks for end-caps. The spatial resolution is $16\text{ }\mu\text{m}$ in $r\text{-}\phi$ for both the barrel and the end-caps. The four complete barrels are positioned in radius of 300, 373, 447 and 520 mm. Tracks can be distinguished if separated by more than $\sim 200\text{ }\mu\text{m}$. There are 6.3 millions readout channels for the SCT.

Transition Radiation Tracker

The TRT occupies the other part of the ID. It consist of 370000 drift tubes called straws, each straw has a diameter of 4 mm and 1.44 m in long. The straws are filled with gas mixture of 70% Xe , 27% CO_2 and 3% O_2 its wall acts as a cathode and kept at high voltage. The anode is a $30\text{ }\mu\text{m}$ diameter plated tungsten wire placed in the center of the straw. When a charged particle traverses a straw, it ionizes the gas and the produced electrons travel through the anode generating an electric signal. To keep the TRT performance to be constant, the close-loop gas system is used maintaining the correct gas fractions. The straws are arranged to be parallel to the beam-pipe in the barrel and perpendicular in the end-cap region. There are about 50k straws in the barrel and 320k straws in the end-cap providing high precision measurement for each track. The radial resolution is about $130\text{ }\mu\text{m}$.

In the Perigee representation, tracks are described using the parameters of a helical trajectory at the point of closest approach to the z-axis: the transverse impact parameter d_0 , the z coordinate z_0 , the angles θ and ϕ and the inverse of the particle momentum multiplied by the charge q/p, as illustrated in Figure 3.11 The expected momentum resolution of the inner detector, without the IBL, is given by:

$$\sigma(1/p_T) \cdot p_T = 0.036\% \cdot p_T[\text{GeV}] \oplus 1.3\%, \quad (3.6)$$

\oplus denote the quadrature addition.

3.2.3 Calorimeter system

Based on the calorimetry, the ATLAS calorimeter system is designed to provide a precise energy and position reconstruction for electromagnetic particles (electrons, photons) and jets (hadrons). The calorimeter also allows to measure the missing transverse energy and provides the separation of electrons and photons from hadrons and jets. The calorimeter system is composed of two calorimeters: the electromagnetic

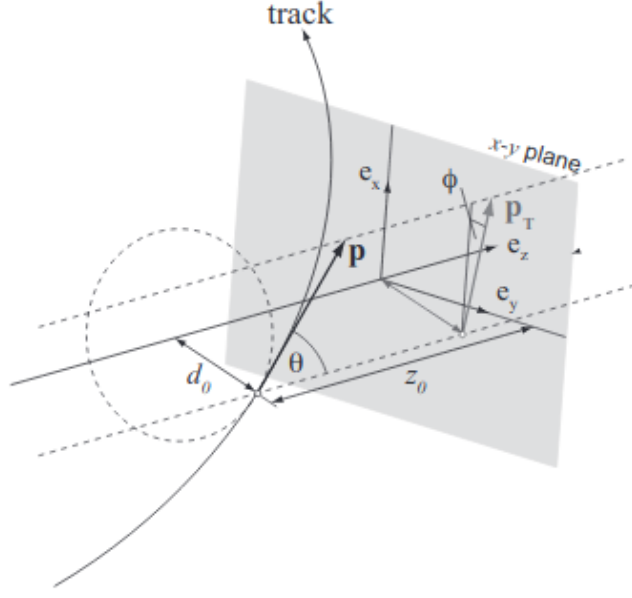


Figure 3.11: The Perigee representation of the track [39].

calorimeter (ECal) and the hadronic calorimeter (HCal). Both of them are sampling calorimeters, with alternating layers of a heavy absorber material and an active material in which an ionisation signal is produced. Figure 3.12 shows a three dimensional view of the ATLAS calorimeter system.

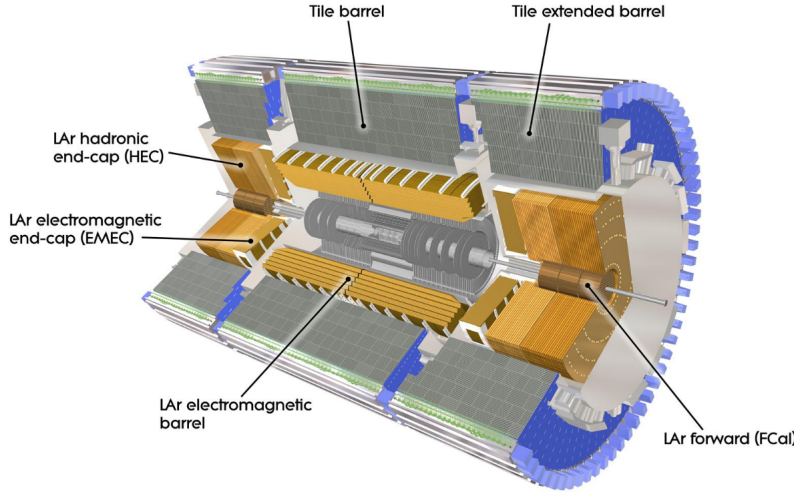


Figure 3.12: ATLAS Calorimeter system.

Electromagnetic calorimeter

The ECal is the first sub-detector after the ID. It is dedicated to reconstructing the energy of electrons and photons exploiting their showers [40]. It covers the region of $|\eta| < 3.2$ excluding the region $1.375 < |\eta| < 1.52$ which correspond to the transition region between the barrel and end-caps. The barrel part covers $|\eta| < 1.475$, while the two end-caps cover $1.375 < |\eta| < 3.2$. The barrel and end-caps are composed of

alternated layers of absorbing material Lead (Z=82), separated by active medium Liquid Argon (LAr). The advantages of LAr, such as radiation hardness, intrinsic linear behaviour, cheapness compared to other noble gases, have been considered to outweigh the difficulties associated with the need of cryostats and signal feed-throughs. The total thickness of the calorimeter is 22 radiation lengths in the barrel, and more than 24 radiation lengths in the end-caps. The radiation lengths X_0 is defined as the scale after which high-energy electrons loose all but 1/e of their initial energy. X_0 of lead is 5.6mm.

Electrons and photons traversing the calorimeters initiate electromagnetic cascades, in which e^+e^- pair production and bremsstrahlung processes occur. High-energy electrons predominantly loose energy in matter through bremsstrahlung, while high-energy photons create e^+e^- . EM particle produce shower when passed through ECal until its energy falls below the critical energy E_c . E_c , can be defined as the energy for which the energy loss per X_0 due to ionisation of the material is equal to the particle energy. In lead, $E_c=7.4$ MeV for electrons. The EM shower ionizes the atom of the liquid Argon generating an electric signal proportional to the energy deposit by the particle. The ionization is drifted to the electrode under electric field generated by the high voltage of 2000 V. To provide a huge signal response and hermiticity, ATLAS Collaboration adopted a particular geometry for the ECal: *accordion* geometry. In the barrel, the accordion waves are axial and run in ϕ ; the folding angles of the waves vary with radius to keep the liquid-argon gap constant and reduce the dead zone. In the end-caps, the waves are parallel to the radial direction and run axially. The size of the drift gap on each side of the electrode is 2.1 mm. Figure 3.13 shows the accordion shape of the EM calorimeter.

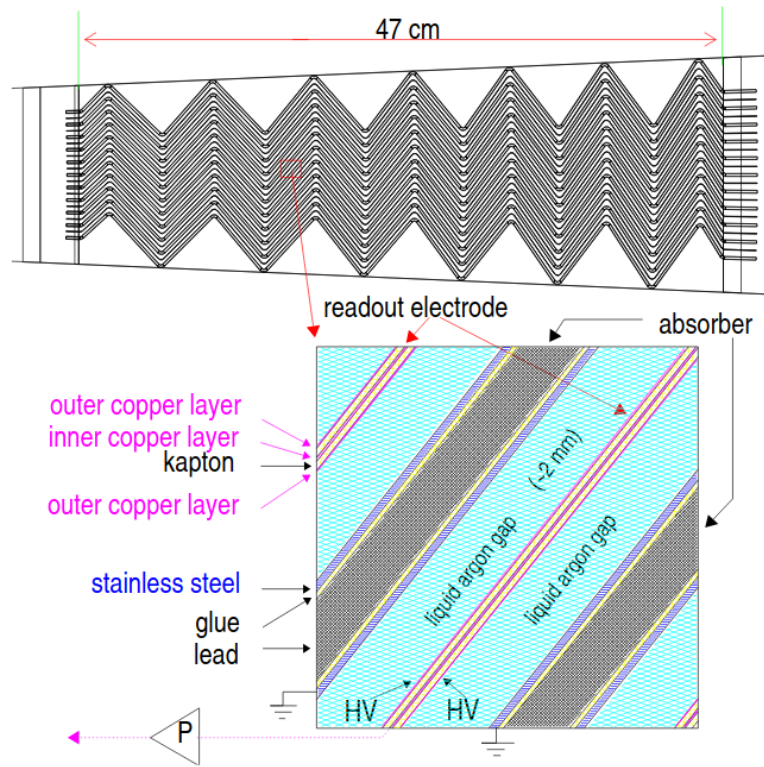


Figure 3.13: Accordion shape of the EM calorimeter.

The ECal is further segmented in three longitudinal layers, to allow to measure the longitudinal shower development called respectively strip, middle and back. It has different EM cells granularity $\Delta\eta \times \Delta\phi$ per layer. Cells of the middle layer (Lr2) in the barrel region are 0.025×0.025 , while for

the strip (Lr1) cells are 8 times finer in the $|\eta|$ direction providing a precise η measurement of incident particles. The back layer (Lr3) cells has a twice coarser granularity in η and the same ϕ segmentation as in Lr2. Before the EM barrel calorimeter there is a Presampler (PS) LAr detector (Lr0), covering range $|\eta| < 1.8$ and placed to start the shower before the calorimeter. PS has the finest granularity with a cell size of $\Delta\eta \times \Delta\phi = 0.003 \times 0.1$ used for $\pi \rightarrow \gamma\gamma$ background separation. The number of samplings and the granularity in each of the samplings are summarized in Table 3.1. Physics studies showed that

Sampling	$ \eta < 1.5$	$1.5 < \eta < 1.8$	$1.8 < \eta < 2.0$	$2.0 < \eta < 2.5$	$2.5 < \eta < 3.2$
Presampling	0.025×0.1	0.025×0.1			
Strip	$0.025/8 \times 0.1$	$0.025/8 \times 0.1$	$0.025/6 \times 0.1$	$0.025/4 \times 0.1$	0.1×0.1
Middle	0.025×0.025	0.025×0.025	0.025×0.025	0.025×0.025	0.1×0.1
Back	0.050×0.025	0.05×0.025	0.05×0.025	0.05×0.025	

Table 3.1: Granularity of the EM calorimeter ($\Delta\eta \times \Delta\phi$) [40].

precision physics can hardly be extended beyond a pseudorapidity of 2.5. For this reason, the small wheel has a coarser granularity and only two samplings in depth. EM calorimeter resolution is given by:

$$\sigma_E/E = \frac{10\%}{E} \oplus 0.17\%. \quad (3.7)$$

Hadronic calorimeter

At high energy colliders, quarks and gluons fragment to a beam of particles called jets (hadronic showering). The Hadronic Calorimeter (HCal) completes the measurement of the jets energy [41]. Hadronic showers are larger than electromagnetic ones, thus it needs to be large enough to contain the hadronic showers and reduce the punch-through hadrons penetrating to the muon system. The total thickness is chosen to be about $11 X_0$ to allows to have good performance on resolution for high energy jets. The hadronic calorimeter is divided into the Tile calorimeter and the LAr hadronic end-caps calorimeter. The barrel calorimeter is made of steel as absorbing material and scintillating plastic tiles as active medium and cover the range $|\eta| < 1$ with two extensions in the range $0.8 < |\eta| < 1.7$. The end-caps cover the range $1.5 < |\eta| < 3.2$ and it is composed of two wheels made of parallel copper plates with LAr as active material in between. For the determination of the missing energy a good hermetic coverage is essential. Therefore ATLAS calorimeter is also equipped with a calorimeter covering the very forward region of $3.1 < |\eta| < 4.9$ the LAr Forward Calorimeter (FCal).

The Tile calorimeter provides signal by the tiles scintillation. The tiles are perpendicular to the beam-pipe with 3 mm thick. It consists of a barrel ($|\eta| < 1.0$) and two extended barrels ($0.8 < |\eta| < 1.7$). The Tile calorimeter is segmented into three layers. The dimension of the cells corresponds to $\Delta\eta \times \Delta\phi = 0.1 \times 0.1$ in first two layers and $\Delta\eta \times \Delta\phi = 0.2 \times 0.1$ in the last layer to contain the hadronic shower. A vertical gap of 68 cm wide between the barrel and extended barrel regions is used for passage of cables from the ID and the EM calorimeter.

LAr cover end-cap and forward regions with $1.5 < |\eta| < 4.9$. Each end-cap calorimeter (HEC) consists of two independent wheels of equal diameter with copper absorber plates. The end-cap calorimeter is divided into front, middle and back longitudinal layers. The FCal is placed at a distance of about 5 meters from the interaction point. It high density detector facing a very high particle flux and consisting of three wheels on each side employing liquid argon as an active material. The innermost wheel is optimized for electromagnetic showers and employs copper as the absorber. While the other two wheels measure hadronic showers using tungsten as absorbing material. The granularity of the hadronic LAr

calorimeter is $\Delta\eta \times \Delta\phi = 0.1 \times 0.1$ for $1.5 < |\eta| < 2.5$ and $\Delta\eta \times \Delta\phi = 0.2 \times 0.2$ for $2.5 < |\eta| < 3.2$ while the forward calorimeter has $\Delta\eta \times \Delta\phi = 0.2 \times 0.2$. The HCal is designed to measure the energy with a resolution of [42]:

$$\sigma_E/E = \frac{50\%}{E} \oplus 3\%. \quad (3.8)$$

3.2.4 Muon Spectrometer

Muons are minimally ionising particles in the detector due to their relatively high mass, therefore are not stopped in the calorimeter. The Muon Spectrometer (MS) is the outermost part of the ATLAS detector dedicated to detect muons exiting the calorimeter and measure their momentum in the range of $|\eta| < 2.7$ [43]. A large superconducting air-cored toroid magnet is used to bend muons trajectories. Over the range $|\eta| < 1.4$, magnetic bending is provided by the large barrel toroid. For $1.6 < |\eta| < 2.7$ region muon tracks are bent by two smaller end-cap magnets inserted into both ends of the barrel toroid. Over $1.4 < |\eta| < 1.6$, usually referred to as the transition region, magnetic deflection is provided by a combination of barrel and end-cap fields. Two different functions are accomplished by the MS: triggering and high precision tracking. The tracking is performed by the Monitored Drift Tubes (MDTs) and by Cathod Strips Chambers (CSCs) at large pseudo-rapidity. However, trigger system covers the region up to $|\eta| < 2.4$, and it is composed by Resistive Plate Chambers (RPCs) in the barrel and Thin Gap Chamber (TGC) in the end-caps. The conceptual layout of the spectrometer is shown in Figures 3.14.

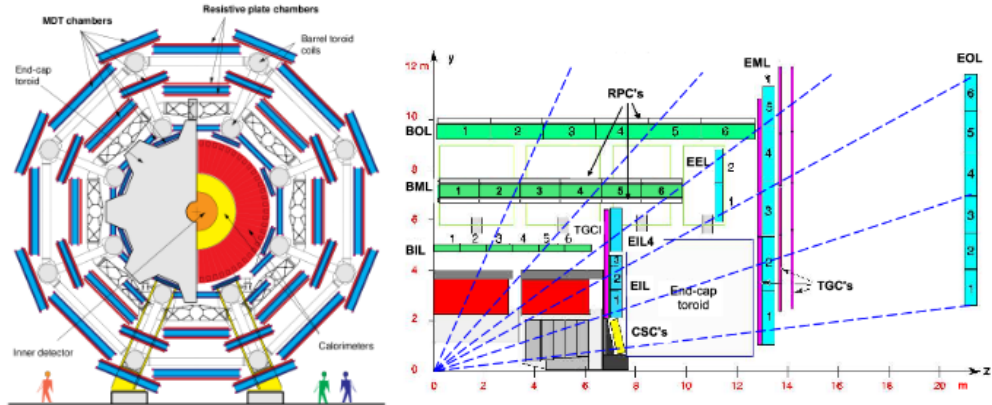


Figure 3.14: Side view of one quadrant (*right*) and transverse view (*left*) of the muon spectrometer.

The Monitored Drift Tubes are aluminium drift tubes with a diameter of 29.970 mm as Figure 3.15 shows, operating with a gas mixture of 93% of Ar and 7% of CO_2 Ar/CO₂ at 3 bar pressure. Each chamber consists of two sections with three (inner station) or four (middle and outer station) layers of the drift tubes. Tungsten-rhenium wire of 50 μ m collects the electrons resulting from ionization at a potential of 3 kV. The maximum drift time can reach about 700 ns. The MDTs are designed for precise tracking of muons and cover most of the MS pseudorapidity total coverage, with a single-hit resolution of about 35 μ m per chamber.

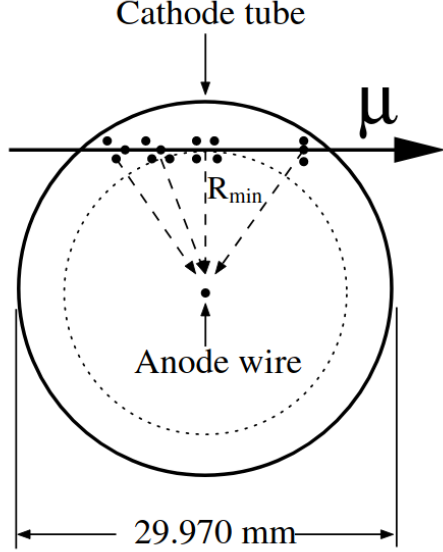


Figure 3.15: Transverse cross section of the MDT tube.

The Cathode-Strip Chambers are multi-wire proportional chambers filled with a mixture of 80% of Ar and 20% of CO_2 with cathode planes segmented into strips in an orthogonal direction to the beam axis. The CSCs cover the range of $2.0 < |\eta| < 2.7$ which is partially covered by the ID and has higher particle flux, because of their better time resolution and rate capability than MDTs. The CSC chambers have a slightly lower resolution than the MDTs, with $40 \mu m$ in the tracks bending plane, and 5 mm in the transverse plane.

For trigger purpose, the RPCs placed in the barrel, covering the range $|\eta| < 1.05$, are arranged into three concentric layers around the beam axis and placed before or after the MDT layers as Figure shows 3.14. The RPC unit is composed of gap of 2 mm formed by two parallel electrodes. The gap is filled with a mixture gas of 94.7% of $C_2H_2F_4$, 5% of $Iso - C_2H_2F_4$ and 0.3% of SF_6 . The electric field between electrodes is about 4.9 kV/mm. The end-caps are equipped with the TGCs up to $|\eta| = 2.4$. The TGCs are multi-wire proportional chambers filled with a mixture 55% of CO_2 and 45% of $n - C_5H_{12}$. The TGCs are arranged in seven layers in each side.

The overall momentum resolution $\frac{\sigma_{p_T}}{p_T}$ provided by the muon system is 4% (1%) at 5GeV (1TeV) [44].

3.2.5 Trigger

Collision rate at the center of ATLAS is 40MHz due to the bunch crossing in each 25 ns provided by LHC. At such a rate, it is technically not possible to fully process and store all data recorded by the ATLAS detector. The ATLAS trigger system was design to handle this problem, the purpose of the trigger system is to reduce the input of 40 MHz bunch crossing rate to an output rate of about 200 Hz in order to record them for further analysis. This is done thanks to two separated trigger systems. The first level so-called Level-1 (L1) [45] is a hardware-based trigger that uses reduced granularity signals from the calorimeter and the muon spectrometer to identify Regions-Of-Interest (ROI) with high energy objects or high multiplicity at a latency of $2.5 \mu s$. The L1 trigger system is responsible for reducing the rate to at least 75 kHz. Events passing the L1 trigger are then sent to the software-based High-Level Trigger (HLT) [46]. At the HLT, a fast analysis of these ROTs followed by an offline-like reconstruction of the events takes place with a processing time of around 0.2 s. The HLT creates output with a frequency of

around 1 kHz. Often the final output rate cannot be made small enough [47]. In this case only random events are selected and stored.

3.3 Physics objects reconstruction

ATLAS provides energy deposits collected by sub-detectors. To interpret this raw output in terms of the event particles an advanced particle reconstruction chains have to be employed. These are described in this Section.

Photons in ATLAS

This include :

- Introduction to electromagnetic objects and shower
- Photon reconstruction
- Photon Isolation
- Photon identification (Run 2 cut based)
- Shower shape mis-modelling
- Convolutional Neural Network for photon identification

4.1 Photons Reconstruction

In this section, I will describe in details the reconstruction of photons and energy calibration.

4.2 Photons Isolation

Photon isolation and different isolation WPs will be discussed here.

4.3 Photons Identification

The identification algorithm will be discussed here, and how the shower shape mis-modelling is affecting the ID efficiency.

4.4 Shower shape mis-modelling

The QT work will fit here.

4.5 Convolutional Neural Network for Photon Identification

The CNN work will fit here to improve the photon identification efficiency and if scale factor are ready by the date of the thesis will be included to.

4.6 Conclusion

A conclusion to the chapter will be discussed here by answering to :

- What is the limits for the current ID method (cut based) ?
- How CNN is improving the ID efficiency ?
- What is the limits of the CNN model ?
- How we can improve the CNN for future ?

Other Objects in ATLAS

This should include the reconstruction and identification of other objects such :

- Electrons
- Muons
- Tracks ?
- MET

This chapter will be merged with detector chapter and LHC

Experimental Setup for Self-coupling measurement

This chapter should include the HH analysis and κ_λ limits

Conclusion

Appendix 1

Bibliography

- [1] M. Tanabashi et al. “Review of Particle Physics”. In: *Phys. Rev. D* 98 (3 2018), p. 030001. DOI: 10.1103/PhysRevD.98.030001. URL: <https://link.aps.org/doi/10.1103/PhysRevD.98.030001>.
- [2] G. Arnison et al. “Experimental observation of isolated large transverse energy electrons with associated missing energy at $s=540$ GeV”. In: *Physics Letters B* 122.1 (1983), pp. 103–116. ISSN: 0370-2693. DOI: [https://doi.org/10.1016/0370-2693\(83\)91177-2](https://doi.org/10.1016/0370-2693(83)91177-2). URL: <http://www.sciencedirect.com/science/article/pii/0370269383911772>.
- [3] P. Bagnaia et al. “Evidence for $Z \rightarrow e^+e^-$ at the CERN pp collider”. In: *Physics Letters B* 129.1 (1983), pp. 130–140. ISSN: 0370-2693. DOI: [https://doi.org/10.1016/0370-2693\(83\)90744-X](https://doi.org/10.1016/0370-2693(83)90744-X). URL: <http://www.sciencedirect.com/science/article/pii/037026938390744X>.
- [4] F. Englert and R. Brout. “Broken Symmetry and the Mass of Gauge Vector Mesons”. In: *Phys. Rev. Lett.* 13 (9 1964), pp. 321–323. DOI: 10.1103/PhysRevLett.13.321. URL: <https://link.aps.org/doi/10.1103/PhysRevLett.13.321>.
- [5] John Ellis, Mary K. Gaillard, and Dimitri V. Nanopoulos. *A Historical Profile of the Higgs Boson*. 2012. arXiv: 1201.6045 [hep-ph].
- [6] David Delgove. “Mesure des propriétés du boson de Higgs avec l’expérience ATLAS au LHC”. Theses. Université Paris-Saclay, 2016. URL: <https://tel.archives-ouvertes.fr/tel-01494070>.
- [7] In: *Physics Letters B* 565 (2003), pp. 61–75. ISSN: 0370-2693. DOI: 10.1016/s0370-2693(03)00614-2. URL: [http://dx.doi.org/10.1016/S0370-2693\(03\)00614-2](http://dx.doi.org/10.1016/S0370-2693(03)00614-2).
- [8] T. Aaltonen et al. “Combination of Tevatron Searches for the Standard Model Higgs Boson in the W+W Decay Mode”. In: *Physical Review Letters* 104.6 (2010). ISSN: 1079-7114. DOI: 10.1103/physrevlett.104.061802. URL: <http://dx.doi.org/10.1103/PhysRevLett.104.061802>.
- [9] ALEPH Collaboration et al. *Precision Electroweak Measurements and Constraints on the Standard Model*. 2009. arXiv: 0911.2604 [hep-ex].
- [10] Sayipjamal Dulat et al. “New parton distribution functions from a global analysis of quantum chromodynamics”. In: *Physical Review D* 93.3 (2016). ISSN: 2470-0029. DOI: 10.1103/physrevd.93.033006. URL: <http://dx.doi.org/10.1103/PhysRevD.93.033006>.
- [11] Sayipjamal Dulat et al. “New parton distribution functions from a global analysis of quantum chromodynamics”. In: *Physical Review D* 93.3 (2016). ISSN: 2470-0029. DOI: 10.1103/physrevd.93.033006. URL: <http://dx.doi.org/10.1103/PhysRevD.93.033006>.
- [12] *LHC Higgs Working Group*. URL: <https://twiki.cern.ch/twiki/bin/view/LHCPhysics/LHCHWG?redirectedfrom=LHCPhysics.LHCHXSWG>.
- [13] S. Dittmaier et al. “Handbook of LHC Higgs Cross Sections: 1. Inclusive Observables”. In: (2011). DOI: 10.5170/CERN-2011-002. arXiv: 1101.0593 [hep-ph].

- [14] S. Dittmaier et al. “Handbook of LHC Higgs Cross Sections: 2. Differential Distributions”. In: (2012). doi: 10.5170/CERN-2012-002. arXiv: 1201.3084 [hep-ph].
- [15] D. de Florian et al. “Handbook of LHC Higgs Cross Sections: 4. Deciphering the Nature of the Higgs Sector”. In: 2/2017 (2016). doi: 10.23731/CYRM-2017-002. arXiv: 1610.07922 [hep-ph].
- [16] G. Aad et al. “Observation of a new particle in the search for the Standard Model Higgs boson with the ATLAS detector at the LHC”. In: *Physics Letters B* 716.1 (2012), pp. 1–29. ISSN: 0370-2693. doi: 10.1016/j.physletb.2012.08.020. URL: <http://dx.doi.org/10.1016/j.physletb.2012.08.020>.
- [17] S. Chatrchyan et al. “Observation of a new boson at a mass of 125 GeV with the CMS experiment at the LHC”. In: *Physics Letters B* 716.1 (2012), pp. 30–61. ISSN: 0370-2693. doi: 10.1016/j.physletb.2012.08.021. URL: <http://dx.doi.org/10.1016/j.physletb.2012.08.021>.
- [18] Aad and *al.* “Combined Measurement of the Higgs Boson Mass in pp Collisions at $\sqrt{s} = 7$ and 8 TeV with the ATLAS and CMS Experiments”. In: *Phys. Rev. Lett.* 114 (19 2015), p. 191803. doi: 10.1103/PhysRevLett.114.191803. URL: <https://link.aps.org/doi/10.1103/PhysRevLett.114.191803>.
- [19] *Measurement of the properties of Higgs boson production at $\sqrt{s}=13$ TeV in the $H \rightarrow \gamma\gamma$ channel using $139 fb^{-1}$ of pp collision data with the ATLAS experiment*. Tech. rep. ATLAS-CONF-2020-026. Geneva: CERN, 2020. URL: <https://cds.cern.ch/record/2725727>.
- [20] D. de Florian et al. *Handbook of LHC Higgs Cross Sections: 4. Deciphering the Nature of the Higgs Sector*. CERN Yellow Reports: Monographs. 869 pages, 295 figures, 248 tables and 1645 citations. Working Group web page: <https://twiki.cern.ch/twiki/bin/view/LHCPhysics/LHCHXSWG>. 2016. doi: 10.23731/CYRM-2017-002. URL: <http://cds.cern.ch/record/2227475>.
- [21] S. Borowka et al. “Higgs Boson Pair Production in Gluon Fusion at Next-to-Leading Order with Full Top-Quark Mass Dependence”. In: *Phys. Rev. Lett.* 117 (1 2016), p. 012001. doi: 10.1103/PhysRevLett.117.012001. URL: <https://link.aps.org/doi/10.1103/PhysRevLett.117.012001>.
- [22] Aaboud et al. “Search for Higgs boson pair production in the $\gamma\gamma b\bar{b}$ final state with 13 TeV pp collision data collected by the ATLAS experiment”. In: (2018). URL: <http://cds.cern.ch/record/2630823>.
- [23] Ilaria Brivio, Yun Jiang, and Michael Trott. “The SMEFTsim package, theory and tools”. In: *Journal of High Energy Physics* 2017.12 (2017). ISSN: 1029-8479. doi: 10.1007/jhep12(2017)070. URL: [http://dx.doi.org/10.1007/JHEP12\(2017\)070](http://dx.doi.org/10.1007/JHEP12(2017)070).
- [24] B. Grzadkowski et al. “Dimension-six terms in the Standard Model Lagrangian”. In: *Journal of High Energy Physics* 2010.10 (2010). ISSN: 1029-8479. doi: 10.1007/jhep10(2010)085. URL: [http://dx.doi.org/10.1007/JHEP10\(2010\)085](http://dx.doi.org/10.1007/JHEP10(2010)085).
- [25] Ilaria Brivio and Michael Trott. “The standard model as an effective field theory”. In: *Physics Reports* 793 (2019), pp. 1–98. ISSN: 0370-1573. doi: 10.1016/j.physrep.2018.11.002. URL: <http://dx.doi.org/10.1016/j.physrep.2018.11.002>.
- [26] Oliver Sim Brüning et al. *LHC Design Report*. CERN Yellow Reports: Monographs. Geneva: CERN, 2004. doi: 10.5170/CERN-2004-003-V-1. URL: <https://cds.cern.ch/record/782076>.
- [27] Cinzia De Melis. “The CERN accelerator complex. Complexe des accélérateurs du CERN”. In: (Jan. 2016). General Photo. URL: <https://cds.cern.ch/record/2119882>.

- [28] The ATLAS Collaboration. *Public luminosity results*. URL: https://twiki.cern.ch/twiki/bin/view/AtlasPublic/LuminosityPublicResultsRun2#Multiple_Year_Collision_Plots.
- [29] The ATLAS Collaboration et al. “The ATLAS Experiment at the CERN Large Hadron Collider”. In: *Journal of Instrumentation* 3.08 (Aug. 2008), S08003–S08003. doi: 10.1088/1748-0221/3/08/s08003. URL: <https://doi.org/10.1088/1748-0221/3/08/s08003>.
- [30] *ATLAS inner detector: Technical Design Report, 1.* Technical design report. ATLAS. Geneva: CERN, 1997. URL: <https://cds.cern.ch/record/331063>.
- [31] Kyungeon Choi. *Tracking and Vertexing with the ATLAS Inner Detector in the LHC Run-2*. Tech. rep. ATL-PHYS-PROC-2017-075. Geneva: CERN, June 2017. doi: 10.1007/978-981-13-1316-5_75. URL: <https://cds.cern.ch/record/2271033>.
- [32] Karolos Potamianos. *The upgraded Pixel detector and the commissioning of the Inner Detector tracking of the ATLAS experiment for Run-2 at the Large Hadron Collider*. Tech. rep. ATL-PHYS-PROC-2016-104. 15 pages, EPS-HEP 2015 Proceedings. Geneva: CERN, Aug. 2016. URL: <https://cds.cern.ch/record/2209070>.
- [33] M Capeans et al. *ATLAS Insertable B-Layer Technical Design Report*. Tech. rep. CERN-LHCC-2010-013. ATLAS-TDR-19. Sept. 2010. URL: <https://cds.cern.ch/record/1291633>.
- [34] ATLAS Collaboration. *Impact Parameter Resolution*. URL: <https://atlas.web.cern.ch/Atlas/GROUPS/PHYSICS/PLLOTS/IDTR-2015-007/>.
- [35] *Timing improvements for the ATLAS offline reconstruction for run-2*. Tech. rep. ATL-SOFT-PUB-2014-004. Geneva: CERN, Oct. 2014. URL: <https://cds.cern.ch/record/1955923>.
- [36] ATLAS Collaboration. *The Optimization of ATLAS Track Reconstruction in Dense Environments*. URL: <https://atlas.web.cern.ch/Atlas/GROUPS/PHYSICS/PUBNOTES/ATL-PHYS-PUB-2015-006/>.
- [37] *Expected performance of the ATLAS b-tagging algorithms in Run-2*. Tech. rep. ATL-PHYS-PUB-2015-022. Geneva: CERN, July 2015. URL: <http://cds.cern.ch/record/2037697>.
- [38] *Commissioning of the ATLAS high-performance b-tagging algorithms in the 7 TeV collision data*. Tech. rep. ATLAS-CONF-2011-102. Geneva: CERN, July 2011. URL: <http://cds.cern.ch/record/1369219>.
- [39] T G Cornelissen et al. *Updates of the ATLAS Tracking Event Data Model (Release 13)*. Tech. rep. ATL-SOFT-PUB-2007-003. ATL-COM-SOFT-2007-008. Geneva: CERN, June 2007. URL: <https://cds.cern.ch/record/1038095>.
- [40] *ATLAS liquid-argon calorimeter: Technical Design Report*. Technical design report. ATLAS. Geneva: CERN, 1996. URL: <https://cds.cern.ch/record/331061>.
- [41] *ATLAS tile calorimeter: Technical Design Report*. Technical design report. ATLAS. Geneva: CERN, 1996. URL: <https://cds.cern.ch/record/331062>.
- [42] A. Hrynevich. “Performance of the ATLAS Tile Calorimeter”. In: *Journal of Instrumentation* 12.06 (June 2017), pp. C06021–C06021. doi: 10.1088/1748-0221/12/06/c06021. URL: <https://doi.org/10.1088/1748-0221/12/06/c06021>.
- [43] *ATLAS muon spectrometer: Technical Design Report*. Technical design report. ATLAS. Geneva: CERN, 1997. URL: <https://cds.cern.ch/record/331068>.
- [44] A. Airapetian et al. *ATLAS detector and physics performance: Technical Design Report, 1.* Technical design report. ATLAS. Geneva: CERN, 1999. URL: <https://cds.cern.ch/record/391176>.

- [45] *ATLAS level-1 trigger: Technical Design Report*. Technical design report. ATLAS. Geneva: CERN, 1998. URL: <https://cds.cern.ch/record/381429>.
- [46] Peter Jenni et al. *ATLAS high-level trigger, data-acquisition and controls: Technical Design Report*. Technical design report. ATLAS. Geneva: CERN, 2003. URL: <https://cds.cern.ch/record/616089>.
- [47] T. Golling et al. “The ATLAS data quality defect database system”. In: *The European Physical Journal C* 72.4 (Apr. 2012). ISSN: 1434-6052. DOI: 10.1140/epjc/s10052-012-1960-y. URL: <http://dx.doi.org/10.1140/epjc/s10052-012-1960-y>.